applied optics

Microphysical characterization of free space optical link due to hydrometeor and fog effects

Saverio Mori[1,2] and Frank S. Marzano[1,2,*]

[1]Department DIET, Sapienza University of Rome, Rome Via Eudossiana 18, 00184 Roma, Italy
[2]Center of Excellence CETEMPS, University of L'Aquila, Via Vetoio, Coppito, L'Aquila, Italy
*Corresponding author: frank.marzano@uniroma1.it

Received 28 April 2015; revised 20 June 2015; accepted 1 July 2015; posted 1 July 2015 (Doc. ID 239931); published 27 July 2015

Free space optics (FSO) channel availability is affected by atmospheric water particles, which may introduce severe path attenuation. A unified microphysically oriented atmospheric particle scattering (MAPS) model is proposed and described to simulate particle scattering effects on FSO links. Atmospheric particles, such as raindrops, graupel particles, and snowflakes, together with fog droplets, are considered. Input data to characterize liquid and frozen water particle size distribution, density, and refractivity are derived from available literature data and measurements. Scattering, absorption, and extinction coefficients as well as the asymmetry factor are numerically simulated for each particle class and then parametrized with respect to particle water content, fall rate, and visibility, spanning from visible to infrared wavelengths. Both single- and multiple-scattering effects are discussed and quantified by using a radiative transfer model for small-angle approximation. MAPS simulations confirm that fog layers are those causing the largest power extinction on FSO links, but also several decibels of attenuation can be attributed to snow and rain conditions. Multiple-scattering effects, especially due to fog droplets, heavy rain, and dry snowflakes, typically tend to reduce the total attenuation by increasing the received power. An estimate of these effects, parameterized to single-scattering extinction, is proposed for near-infrared FSO link design.

OCIS codes: (010.1300) Atmospheric propagation; (010.1310) Atmospheric scattering; (060.2605) Free-space optical communication; (010.5620) Radiative transfer; (290.4210) Multiple scattering; (290.5825) Scattering theory.

http://dx.doi.org/10.1364/AO.54.006787

1. INTRODUCTION

Today, society worldwide is prompted by an increased request for information transmission and mobile connectivity. This is one of main reasons for the wireless technology explosion in recent years. Radio frequency (RF) devices and systems constitute most of the current wireless systems, but their capacity is limited by the available fractional bandwidth and overcrowded exploitation of RF spectrum, while frequency allocation fees tend to further raise the overall system costs. In this context the use of optical bands of the electromagnetic (e.m.) spectrum represents an attractive possibility for free space links [1]. Optical wireless communications (OWC) systems, both indoor and outdoor, allow higher bandwidth capacity, robustness to e.m. interference, high spatial confinement, near unlimited reuse, inherent security, and low power consumption; moreover, the optical band is free and not regulated [2]. Nevertheless, the transmission of modulated near-infrared (NIR) beams through the atmosphere, often indicated as free space optics (FSO), is more frequently used to set up optical communications and to interconnect optical fiber networks [3].

The rationale of NIR FSO is the transmission of collimated light beams using low-power NIR lasers. A receiving lens intercepts the FSO collimated beam and focuses photons on a highly sensitive detector. By using single-mode fibers directly as light launchers and light collectors, the conversion of the optical radiation into the electrical domain can be bypassed, and an all-optical treatment of the information can be fully exploited [4]. As long as there is a clear line of sight between the optical source and receiver and sufficient channel margin, optical wireless systems can cover distances of several kilometers [5–9]. Ranges up to 5 km have been tested, even though higher quality of service (QoS) performance may be achieved for shorter link ranges.

Sensitivity to atmospheric phenomena is the principal limitation to FSO systems: atmospheric particles, due to their composition and random dimensional distribution with respect to wavelength, may introduce severe path attenuations, mainly due to scattering properties (absorption is usually negligible at FSO frequencies), on the transmitted signal, up to link interruption. Fog is the most dangerous one because of its high

optical thickness and strong scattering due to particle sizes comparable to the NIR transmission wavelength. In the reasonable hypothesis of spherical particles, fog optical attenuation can be accurately computed applying the Mie scattering theory, once we know the particle size distribution (PSD) and refraction index. Snow and graupel particle effects are also important in terms of optical extinction, whereas effects due to rain are more reduced (e.g., [10]). Another major cause of channel impairment is scintillation, due to the fluctuations of air refraction index and cause of beam wandering and beam spreading; temperature and wind may significantly influence scintillation [11].

With respect to radio frequency (RF) communications, whose history began more than a century ago, FSO is a relatively young technology, started about 30 years ago, and most of the work has been carried out in the last 10–15 years. For this reason, only a few parametric propagation models are available for use in FSO. These models tend to distinguish themselves according to the accounted atmospheric effect. Channel modeling is always an important step to improve the transmission technologies and to counteract atmospheric influences. Nevertheless, the validity of the developed model has to be assessed by proper measurements campaigns.

Several experimental setups have been realized (see, e.g., [5,6,12–14]), and several measurement campaigns have been performed to evaluate hydrometeor effects upon FSO links. Awan *et al.* [15] carried out two campaigns in which fog (maritime and continental) specific attenuation was determined by visibility measurements. In this respect, it worth noticing that path attenuation estimated by visibility, usually by means of empirical formulas, is usually much greater than the dynamic range of the optical receiver. Awan *et al.* [6] reported a campaign in which fog-specific attenuation is measured with peak values of 224 dB/km. Nebuloni and Capsoni [10,16] analyzed rain and snow effects on a FSO link demonstrating that a laser beam traveling through falling snow may undergo attenuation levels often in excess of 45 dB/km, whereas fades produced by rain rarely exceed 25 dB/km. Kvicera *et al.* [14] analyzed the feasibility of a hybrid FSO/RF link. Finally, several authors (e.g., [11,17–20]) analyzed turbulence effects on a FSO link. A joint project to characterize FSO links by both modeling and experimental perspectives has been carried out in the Rome area (Italy), operating at 1550 nm, together with video and meteorological instruments [12].

This work is devoted to a systematic model analysis of the absorption and scattering effects due to fog droplets and hydrometeor particles such as raindrops, graupel, hail, and snow in a wide range of FSO wavelengths. Input data to characterize the water and frozen PSD and refractivity are derived from the available literature and measurements (Section 2). The proposed microphysically oriented atmospheric particle scattering (MAPS) model can span from visible to infrared wavelengths. The goal is also to provide a generalized parametric characterization of extinction, scattering, asymmetry, and volumetric albedo as a function of water content, atmospheric visibility, and fall rate (Section 3). The single-scattering hypothesis will first be adopted, but multiple-scattering effects will also be discussed in order to explain the apparent extinction through a slab of randomly dispersed particles (Section 4). Conclusions will be drawn in Section 5.

2. HYDROMETEOR CHARACTERIZATION

The main uncertainty in designing an outdoor short-range optical wireless link is the atmospheric attenuation caused by the absorption and scattering by particles. Excluding solid particulates and other aerosols (not considered in this work), water particles, oxygen, and carbon dioxide are mainly responsible for absorption, whereas fog, rain, and snow cause the scattering of optical signals transmitted in free space. This so-called forward scattering process causes the emitted light beam to deflect away from the intended receiver.

While molecular absorption is a selective phenomenon and can be avoided with a proper choice of the FSO carrier (e.g., [21]), scattering and absorption due to hydrometeors and fog always exist and rely on particle characteristics (e.g., size, shape, density, and concentration). In the following paragraphs, the FSO MAPS model for such effects will be illustrated.

A. Hydrometeor Microphysical Parameterization

Atmospheric hydrometeors can have various shapes depending on their microphysics and thermodynamical development (liquid, ice, or mixed phase). For fog droplets (few micrometers in diameter) and small raindrops (less than 1 mm in diameter) it is reasonable to assume a spherical shape with pure water phase with a specific density of 1 $g \cdot cm^{-3}$. The spherical shape is also a common choice for ice particles such as graupel and small hail, whose density is between 0.15 $g \cdot cm^{-3}$ (soft ice) and 0.9 $g \cdot cm^{-3}$ (pure ice) [22,23].

For raindrops larger than 1 mm, the shape tends to oscillate around an oblate form up to about 8 mm diameter, beyond which the break-up phenomenon takes place. Moreover, the snow particles may assume several shapes, starting from aligned vertical ice crystals up to horizontally oriented dendrites [24,25]. For simplicity of treatment, nonspherical particles have been modeled as equi-volume spherical ones. This assumption should not lead to significant errors if we limit our analysis to the statistical features of FSO unpolarized radiation intensity and disregard cross-polarization effects, whose analysis is beyond the scope of this work. Snow particles' density has been derived by particle radius using the model of Brandes *et al.* [26].

Water particles can be distinguished and grouped according to their bulk characteristics and their statistical variability. These include minimum and maximum radius, density, size distribution, effective radius, mass concentration variability, shape parameter, fall velocity, and dielectric constant model. Water particle classes, considered here, are advection fog, radiation fog, light rain, moderate rain, heavy rain, graupel/small hail, dry snow, and wet snow. All of them are referenced in [23], except fog. The formation of a fog layer requires the presence of a sufficient number of condensation nuclei and can occur when air becomes nearly saturated with respect to water vapor (so that relative humidity is close to 100%). Saturation can be produced either by mixing of air masses with different temperature and/or humidity (advection fogs) or by air cooling up to the dew point temperature (radiation fogs) [27]. The advection

Table 1. Microphysical Parameter Variability and Scaled Gamma PSD Parameterization for Atmospheric Particles and Hydrometeors (Fog, Rain, Snow, Graupel) in Different Regimes[a]

Class	$\rho_{p\,\min} \le \rho_p \le \rho_{p\,\max}$ [g · cm^{-3}]	T [K]	$r_{\min} \le r \le r_{\max}$ [mm]	$W_{p\,\min} \le W_p \le W_{p\,\max}$ [g · m^{-3}]	$r_{e\,\min} \le r_e \le r_{e\,\max}$ [mm]	$\mu_{\min} \le \mu_e \le \mu_{\max}$ [adim]	$N_{e\,\min} \le \mathrm{Ne} \le N_{e\,\max}$ [mm^{-1} m^{-3}]	$\Lambda_{e\,\min} \le \Lambda_e \le \Lambda_{e\,\max}$ [adim]
LR, light rain	1.0–1.0	298	0.3/3.5	0.0/0.1	0.1/0.6	0.0/0.1	$9.86 \cdot 10^{-2}/2.43 \cdot 10^{6}$	3.00/3.10
MR, moderate rain	1.0–1.0	298	0.3/3.5	0.0/0.6	0.4/0.8	0.0/0.6	$8.32 \cdot 10^{1}/1.18 \cdot 10^{5}$	3.00/3.60
HR, heavy rain	1.0–1.0	298	0.3/3.5	0.0/5.0	0.6/1.3	0.0/0.8	$2.29 \cdot 10^{1}/1.94 \cdot 10^{5}$	3.00/3.80
G/SH, graupel	0.4–0.4	273	0.5/2.5	0.0/2.5	0.8/2.5	0.0/0.0	$2.26 \cdot 10^{0}/4.66 \cdot 10^{4}$	3.00/3.00
DS, dry snow	0.01–0.2	273	0.5/7.5	0.0/1.0	0.7/1.0	0.0/0.0	$1.20 \cdot 10^{1}/8.48 \cdot 10^{5}$	3.00/3.00
WS, wet snow	0.01–2.0	273	0.5/7.5	0.0/1.0	0.7/1.0	0.0/0.0	$2.24 \cdot 10^{1}/1.10 \cdot 10^{6}$	3.00/3.00
AF, advection fog	1.0–1.0	298	0.0/0.04	0.0/0.4	0.019/0.021	2.9/3.1	$8.31 \cdot 10^{7}/2.86 \cdot 10^{11}$	5.90/6.10
RF, radiation fog	1.0–1.0	298	0.0/0.04	0.0/0.025	0.001/0.006	1.0/5.0	$2.45 \cdot 10^{9}/6.00 \cdot 10^{15}$	4.01/8.00

[a]See Appendices A and B for details.

fog is typical of the maritime environment, while the radiation fog of a continental one.

The main microphysical and dielectric characteristics of the considered hydrometeors are schematically summarized in Table 1 and discussed in the following paragraphs.

B. Hydrometeor Size Distribution

Several authors over the last few decades have studied the hydrometeor size distribution and proposed numerous models. These models usually distinguish among ice particles, raindrops, and fog droplets, and commonly adopted models are the exponential distribution for ice particles, the power law for fog droplets, and the Gamma distribution for raindrops [28].

In this work, we have adopted the scaled-Gamma (SG) particle size distribution (PSD) as a general model for water particles. The SG-PSD model $N_p(r)$ for a generic class of particles p can be written as

$$N_p(r) = N_e \left(\frac{r}{r_e}\right)^{\mu_e} e^{-\Lambda_e\left(\frac{r}{r_e}\right)}, \tag{1}$$

where r [mm] is the volume-equivalent spherical radius and r_e [mm] is the effective radius.

The effective particle number concentration N_e and the "slope" parameter Λ_e in a logarithmic plane are related to the PSD "shape" parameter μ_e through

$$\begin{cases} N_e = 10^3 W_p \frac{3\Lambda_e^{4+\mu_e}}{4\pi\rho_p} \frac{1}{r_e^4} \frac{1}{\Gamma(\mu_e+4)} \\ \Lambda_e = \frac{\Gamma(\mu_e+4)}{\Gamma(\mu_e+3)} \end{cases} \tag{2}$$

with W_p [g · m^{-3}] the mass concentration and ρ_p [g · cm^{-3}] the specific density. Therefore, N_e is [mm^{-1} · m^{-3}] and Λ_e is adimensional. The theoretical background of PSD modeling and the definition of its physical parameters are discussed in Appendix A.

It is worth mentioning that $N_p(r)$ for a given hydrometeor class is completely specified by the three parameters: μ_e, r_e, and W_p (assuming a constant specific density ρ_p). The minimum and maximum radii r_m and r_M, respectively, are also important values to be assigned. The PSD parameter ranges for the selected classes are reported in Table 1. The derived parameters Λ_e, N_e have been obtained by analyzing a set of 1000 simulated PSDs for each class, produced by uniform random generation of μ_e, r_e, and W_p. Variability ranges of the independent parameters μ_e, r_e, and W_p have been chosen with the following criteria. For ice graupel particles and raindrops, characterized by the median volume diameter D_0 [mm], we have derived these parameters by the corresponding PSDs indicated in [23] (their Table 1). Fog particles have been modeled according to [29] (their Fig. 1), while data from [27] (their Table 7) have been considered for comparison. Finally snow particles have been modeled according to [10] (their Fig. 2), using data from [23] for comparison.

As an example, Fig. 1 shows the size distribution for fog (advective and radiative), rain (light, moderate and heavy), graupel, and snow (wet and dry) having set W_p to its mean and maximum values [note that for $W_p = 0$, using Eq. (2), $N_p(r) \equiv 0$ for all radii]. The raindrop distributions show good agreement with [30] (their Fig. 2) and [31] (their Fig. 1), while the fog droplet behavior is in agreement with [6] (their Fig. 4),

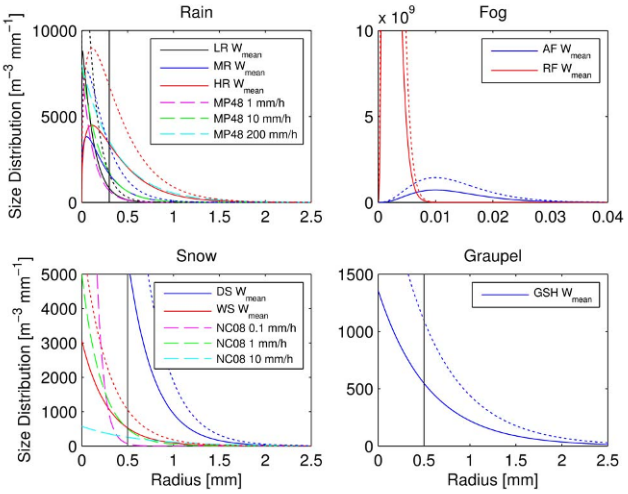

Fig. 1. Average (continuous line) and maximum (dotted line) scaled-Gamma PSDs for fog (advective, AF; radiative, RF), rain (light, LR; moderate, MR; heavy, HR), graupel (GSH), and snow (wet, WS; dry, DS) particles as derived from Table 1. Vertical black line indicates the minimum radius supposed for the hydrometeor classes. Rain panel shows a comparison with Marshall–Palmer (MP48) distribution, while snow one shows a comparison with Sekhon–Srivastava model of [32] (NC08), both for three different precipitation rates (dashed lines). Note the overlap between SG-PSD and MP48/NC08 lines.

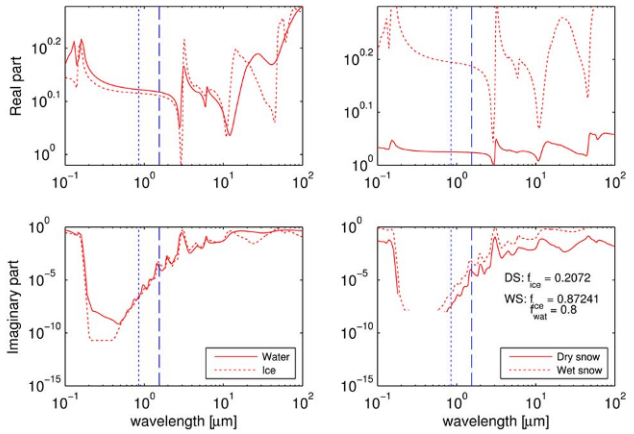

Fig. 2. Real and imaginary parts of water refractive index against wavelength [μm]. Left panels show the complex refractive index for water in liquid and frozen phase. Right panels show the complex refractive index of dry snow and wet snow, obtained using Maxwell–Garnett approximations (DS as a mixture of air and ice; WS as a mixture of air, ice, and water; fractions of inclusion f_i indicated). The vertical blue line indicates the 850 [nm] and 1550 [nm] wavelengths. The imaginary refractivity of snow shows a lack of data for visible wavelengths.

where several fog classes are considered. The raindrop size distributions are compared with the Marshall–Palmer one for several rain rates—and the same for snow particles with respect to the Sekhon–Srivastava model as indicated in [32].

C. Hydrometeor Dielectric Properties

Refractive index modeling for liquid water and ice in the optical spectrum is critical to assess the role of water droplets. In particular, the imaginary part is a measure of the electromagnetic absorption due to particles.

Figure 2 shows the real and imaginary parts of the water refractive index versus wavelength (between optical and thermal infrared bands) for liquid [33] and ice [34] phase as well as for the mixtures of dry snow and wet snow. The imaginary part values are in good agreement with [35] as well. The blue lines in Fig. 2 indicate the 850 and 1550 nm wavelengths, commonly used in FSO communications and hereafter considered, in particular the second, for scattering analysis. Modeling of the refractive index for mixtures has been accomplished using the Maxwell–Garnett approximation [36] (see Appendix B). Dry snow is modeled as a mixture of ice within air with a fraction of inclusion of ~0.2. Wet snow is modeled as a mixture of ice and water within air, with fraction of inclusion of ~0.87 and ~0.8, respectively.

In this work we have considered only water particles, while in real clear air organic and inorganic aerosols are also present. In this respect recent physical-chemical analyses of fog (whose dimensions are comparable with these particles) have been carried out [37]. These works, relative to an area affected by intense industrial and agricultural activities (Po valley, Italy), have shown that for the FSO frequencies of interest the influence of nonwater particles on the complex refraction index is almost negligible. The analysis of aerosol effects is, however, beyond the scope of this paper.

3. HYDROMETEOR SINGLE-SCATTERING EFFECTS

An atmosphere with clouds and rain can be modeled as an absorbing and scattering medium, characterized by a polydispersion of hydrometeors having different size, composition, and shape. Due to the hydrometeor dimensions, comparable with the carrier wavelength, a full scattering matrix approach is required [22]. In the case of spherical particles, the Mie theory can be conveniently used.

Single-scattering optical parameters will first be defined and then simulated at NIR for the various hydrometer classes, identified in Table 1. Statistical parametric models, based on MAPS simulations, will be developed and discussed as well.

A. Single-Scattering Optical Parameters

If e.m. scattering is azimuthally symmetric (as in the case of spherical particles), the volumetric scattering phase function p can be defined as [38]

$$p(\hat{\mathbf{s}}, \hat{\mathbf{s}}') \equiv \frac{k_d(\hat{\mathbf{s}}, \hat{\mathbf{s}}')}{k_s} = \frac{k_d(\hat{\mathbf{s}}, \hat{\mathbf{s}}')}{\int_{4\pi} k_d(\hat{\mathbf{s}}, \hat{\mathbf{s}}')\mathrm{d}\Omega'}, \tag{3}$$

where k_d is the volumetric differential scattering coefficient, k_s is the scattering coefficient, and $d\Omega = \sin\theta d\theta d\phi$ is the solid angle in spherical coordinates (θ, ϕ), whereas $\hat{\mathbf{s}}$ and $\hat{\mathbf{s}}'$ are direction unit vectors along incident angles (θ, ϕ) and scattering angles (θ', ϕ'), respectively. In Eq. (3) the phase function p is evidently normalized to 1. The k_d parameter characterizes the angular distribution of the scattered light, indicating the amount of light, for unit incident irradiance, scattered in a solid unit angle about a given direction. If the angular scattering

phase function p is known, then its first moment is expressed by the *asymmetry factor* g (average cosine of the scattering angle) as follows (e.g., [39,40]):

$$g(\hat{\mathbf{s}}) \equiv \int_{4\pi} (\hat{\mathbf{s}} \cdot \hat{\mathbf{s}}') p(\hat{\mathbf{s}}, \hat{\mathbf{s}}') \mathrm{d}\Omega'. \tag{4}$$

The asymmetry factor ranges between −1 and +1, indicating dominant backward and forward scattering, respectively. If $g = 0$, then scattering is angularly isotropic.

At a given frequency ν and for unpolarized radiation, the volumetric *extinction coefficient* k_e is defined as (e.g., [41])

$$\begin{aligned} k_e \equiv k_a + k_s &= \int_{r_m}^{r_M} \sigma_e(r) N_p(r) \mathrm{d}r \\ &= \int_{r_m}^{r_M} [\sigma_a(r) + \sigma_s(r)] N_p(r) \mathrm{d}r, \end{aligned} \tag{5}$$

where k_a and k_s are the volumetric absorption and scattering coefficients, respectively, while $N_p(r)$ is the SG-PSD defined in Eq. (1). The parameters σ_e, σ_a, and σ_s are the extinction, absorption, and scattering cross sections, respectively; the corresponding extinction, absorption, and scattering efficiencies are defined as $\xi_e = \sigma_e/\pi r^2$, $\xi_a = \sigma_a/\pi r^2$, and $\xi_s = \sigma_s/\pi r^2$. Sometimes the extinction, absorption, and scattering coefficients are indicated by α if expressed in decibel scale, i.e., $\alpha_e = 4.343\ k_e$.

The volumetric *albedo* w is defined as the ratio of the scattering coefficient k_s versus the extinction one k_e (that accounts for both scattering and absorption):

$$w \equiv \frac{k_s}{k_e} = \frac{\int_{r_m}^{r_M} \xi_s(r) \pi r^2 N_p(r) \mathrm{d}r}{\int_{r_m}^{r_M} \xi_e(r) \pi r^2 N_p(r) \mathrm{d}r}. \tag{6}$$

The volumetric albedo w is substantially a measure of scattering efficiency; i.e., a nonscattering atmosphere has a null albedo.

The atmospheric optical parameters k_e, w, and p, or its moment g, can be computed once the properties of the hydrometeor polydispersion are known. In particular, as indicated in [38], efficiencies can be computed by the complex refractive index of the particle and the ratio of particle radius and wavelength only. In this work all hydrometeors have been supposed to be spherically volume-equivalent so that the Mie scattering theory can apply. Even though this approximation may be not suitable for oblate raindrops and complex ice snowflakes, it provides a theoretical common framework in which shape effects can be evaluated as a second-order refinement [22]. Moreover, the unpolarized total radiation we deal with is less sensitive to these shape effects. The e.m. radiation, impinging on the receiving lens, will be the result of the extinction, emission, and scattering processes within traveled atmosphere [42].

Figure 3 shows the extinction efficiency ξ_e, absorption efficiency ξ_a, scattering efficiency ξ_s, and asymmetry factor g for a single particle, for both liquid and frozen phases. It is worth noticing that at the considered wavelengths the ice absorption efficiency is greater than the liquid water one. For comparison, dry particles, such as soot, show a mean single-scattering albedo of 0.835, a mean complex refractive index of 1.51 – j0.026, and a mean asymmetry of 0.39 [43].

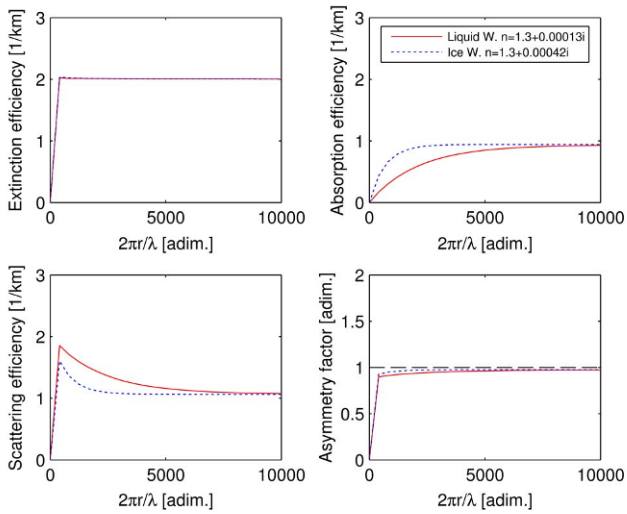

Fig. 3. Mie efficiencies (extinction ξ_e, absorption ξ_a, scattering ξ_s, and asymmetry factor g) for a single spherical water particle, both in liquid phase and in frozen phase (complex refraction index n indicated). Plots have been computed considering a wavelength of 1550 [nm] and a particle radius ranging 0/8 [mm]; the last corresponds to a maximum abscissa of ∼32, 500, truncated at 10,000 because of saturation.

B. Correlation with Water Content

The variability of the microphysical parameters is subject to the meteorological state of the atmosphere whose average thermodynamical features are seasonally and geographically dependent. Indeed, it would be very effective to develop physically based parametric techniques to estimate optical parameters as a function of microphysical properties such as water content and fall rate. A Monte Carlo approach would consist in defining the statistical variability of each microphysical parameter within prescribed bounds, derived from both literature and experimental measurements. The further step should be to assume each optical parameter as a random variable with a given probability density function (PDF) and then compute the optical parameters at NIR as dependent random processes using the models described in Section 3.A. Table 1 summarizes this statistical characterization, supposing each random microphysical parameter uniformly distributed within a given range and uncorrelated with the others.

Figure 4 shows the extinction coefficient α_e [dB/km], scattering coefficient α_s [dB/km], albedo w, and asymmetry factor g, simulated by means of the MAPS model at 1550 nm, for fog particles against particle water content W_p [g · m^{-3}]. As mentioned, we have uniformely varied r_e, μ_e, and W_p under the constraints of Table 1, keeping W_p as the leading variable. The asymmetry parameter is represented in the form $k_s . g$ for spherical particles, as indicated in [38]. Simulated values are comparable with those shown in [27]. Figures 5, 6, and 7 show the same as in Fig. 4, but for raindrops, graupel particles, and snowflakes, respectively. For snow particles, the extinction results are compared with those discussed by [32], showing fairly good consistency.

Previous plots can justify the choice of a power-law regression model of the optical parameters for the pth particle (i.e., fog, rain, graupel, and snow):

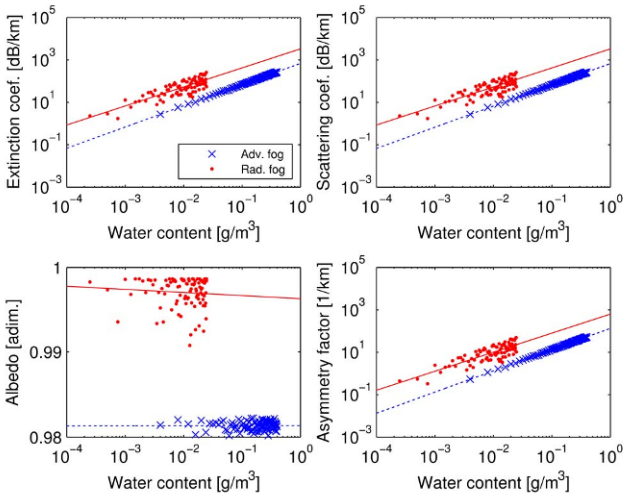

Fig. 4. Fog simulated Mie coefficients (extinction α_e [dB/km], scattering α_s [dB/km], albedo w [adim.], and asymmetry $k_s \cdot g$ [km^{-1}]) as a function of water content W_p [g $\cdot$ m^{-3}] under the model constrained variability and wavelength of 1550 nm (logarithmic scale). Panels show power-law regression curves according to Eq. (7) and Table 2 in Appendix C.

$$\begin{cases} k_e = a_{kep} W_p^{b_{kep}} \\ k_s = a_{ksp} W_p^{b_{ksp}} \\ k_a = a_{kap} W_p^{b_{kap}} \\ k_s \cdot g = a_{gp} W_p^{b_{gp}} \\ w = a_{ksp} W_p^{b_{ksp}} / a_{kep} W_p^{b_{kep}} \end{cases}, \tag{7}$$

where a_X and b_X are the particle- and frequency-dependent regression coefficients. Numerical tests have proved that a power-law model for all four optical parameters at NIR is the best predictor in terms of minimum root mean square error.

Table 2 in Appendix C provides the regression coefficients of optical parameters versus water content for the particles of Table 1 at NIR. Figures 4, 5, 6, and 7 show the relative regression curves. As a further verification, the estimated fog extinction

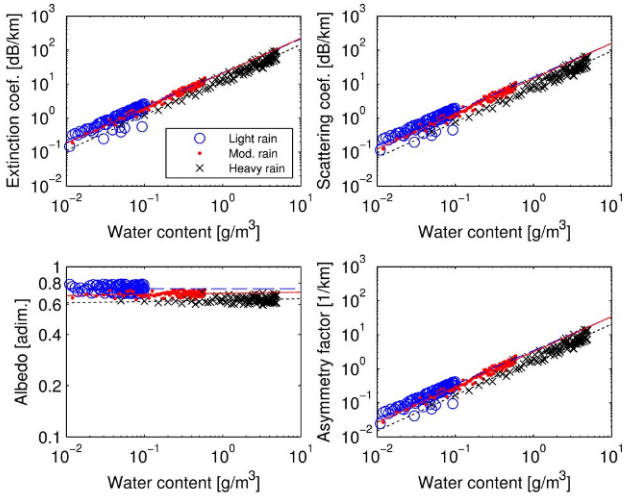

Fig. 5. Same as Fig. 4, but for raindrops.

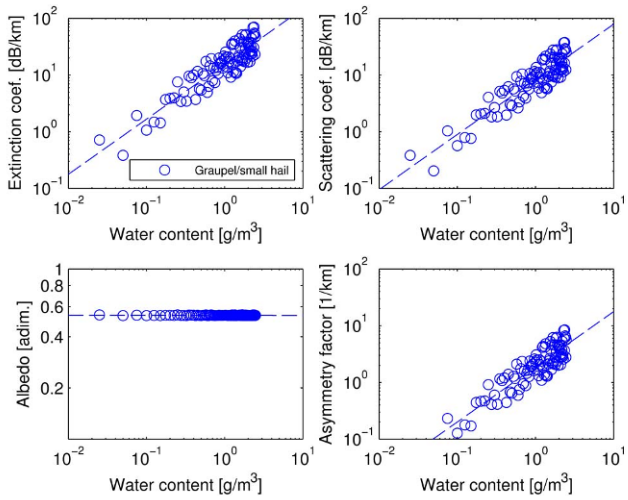

Fig. 6. Same as Fig. 4, but for graupel particles.

coefficients at 0.55, 1.2, 4, and 11 μm, and the estimated fog absorption coefficients at 3.8 and 9.5 μm, have been compared to available models (e.g., [44]), finding good consistency.

The proposed MAPS model is quite flexible and adaptable, allowing the selection of the carrier wavelength. In this respect, Table 2 shows regression coefficients for five different wavelengths. Together with the 1550 nm one, we have considered the wavelengths at 850 nm, currently used in many installations (e.g., [14,29]), at 785 nm (e.g., [10]), at 1064 nm (e.g., [45]), and finally at 10,000 nm as examples of the larger wavelengths that are the subject of renewed feasibility studies (e.g., [46]).

C. Correlation with Particle Fall Rate

The same parametric approach to estimate optical parameters, as in Eq. (7), can be applied by considering the particle fall rate R_p [mm/h] instead of water content W_p. This approach is suitable only for precipitating hydrometeors, but not for fog droplets due to their suspended nature. The rain rate is expressed by means of [47]

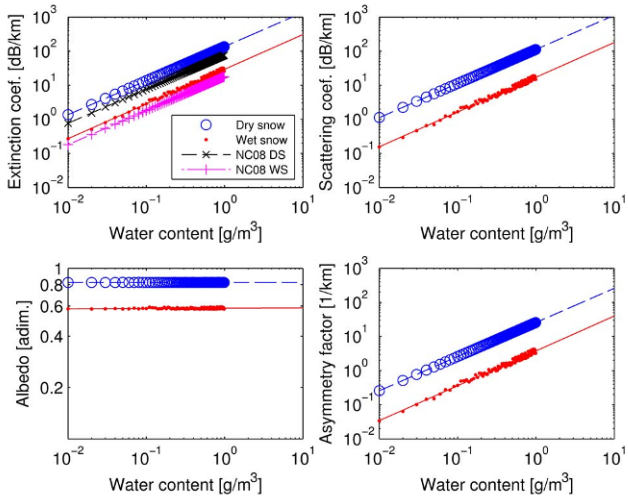

Fig. 7. Same as Fig. 4, but for snowflakes. Extinction panel shows a comparison with the Nebuloni and Capsoni model (NC08) [32].

$$R_p = \int_{r_m}^{r_M} v_p(r)\frac{m_p(r)}{\rho_p}N_p(r)\mathrm{d}r = \int_{r_m}^{r_M}(a_p r^{b_p})\frac{4}{3}\pi r^3 N_p(r)\mathrm{d}r, \quad (8)$$

where v_p is the power-law velocity model and particle mass m_p has been attributed to spherical particles with density ρ_p [48]. Note that the snowfall rate has been estimated using the mass model of [49] and the terminal velocity model of [49,50] for dry snow and wet snow, respectively. An example of the graupel terminal velocity model is reported in [51].

Figures 8 and 9 show the same as in Figs. 5 and 7, respectively, for rain and snow particles, but against precipitation rate. In Fig. 8 the rain extinction panel shows a comparison with the empirical law due to Carbonneau and Wisely [4] and the regression law of Olsen *et al.* [52]. An analogous comparison for snowfall rate is shown in Fig. 9, where results have been performed with respect to [32]. Simulation results have been compared with those from the literature, denoting fairly good agreement (e.g., Fig. 5 in [31], Fig. 5 in [53] for rain, and Fig. 1 of [32] for snow). Simulations for light, moderate, and heavy rainfall tend to follow the Carbonneau–Wisely model variability, whereas the systematic differences for snowfall models are about 0.5 dB/km higher for wet snow and 5 dB/km higher for dry snow mainly due to the adopted different density-diameter model.

Regression parametric models of optical parameters with respect to precipitation rate for rain and snow using the same power-law model of Eq. (7), but where W_p is replaced by R_p [mm/h], can be derived, but are omitted for brevity.

D. Analysis in Terms of Optical Visibility

Let us consider an atmospheric slab of thickness H between the initial level at $z = 0$ and the final level at $z = H$. The z coordinate may represent the coordinate along the optical link, which is supposed to be embedded in a homogeneous random medium of scattering particles. The *optical thickness* τ at frequency ν can be defined as (e.g.,[41])

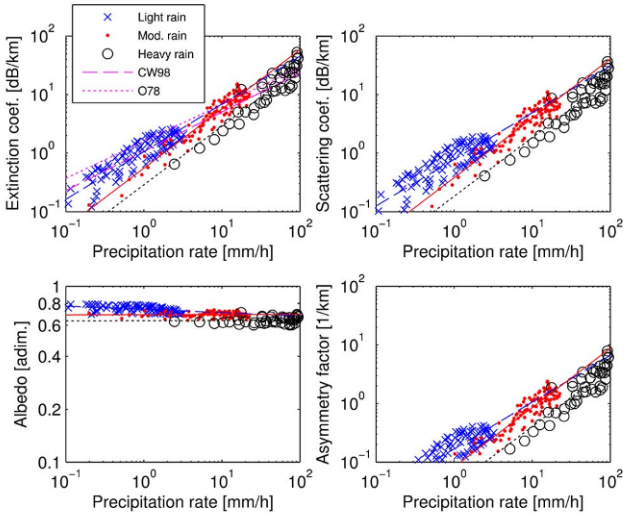

Fig. 8. Same as in Fig. 5, but with respect to precipitation rate R_p [mm/h]. Extinction panel shows a comparison with the Carbonneau and Wisely [4] empirical model (CW98) and the Olsen *et al.* [52] regression model (O78).

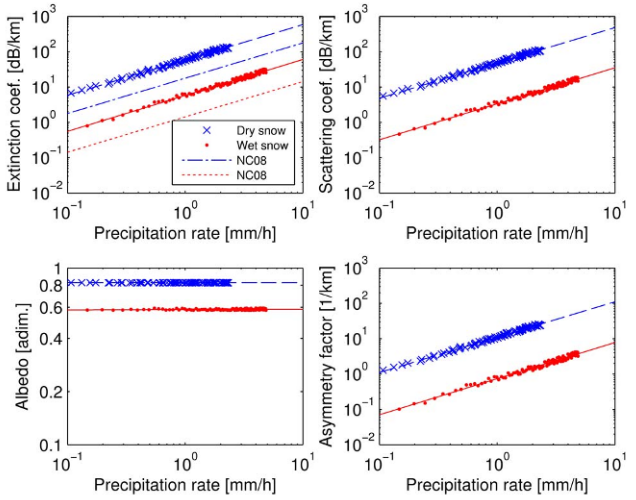

Fig. 9. Same as in Fig. 7, but with respect to precipitation rate R_p [mm/h]. In the top left panel we show a comparison with the parametric model of Nebuloni and Capsoni [32] (NC08).

$$\tau(0,z) \equiv \int_0^z k_e(z')\mathrm{d}z' = \int_0^z [k_s(z') + k_a(z')]\mathrm{d}z' \quad (9)$$

with $\tau = 0$ at $z = 0$, $\tau = \tau_H$ at $z = H$, and k_e generally dependent on z. The *path attenuation* A [dB] is usually the optical thickness expressed in decibels, i.e., $A = 10\log_{10}(\tau)$. For simplicity of notation, we have dropped the frequency dependence of optical parameters.

In general, the extinction law for any electromagnetic unpolarized radiation intensity $I(\mathbf{r}, \hat{\mathbf{s}})$, expressed in $\mathrm{W}\cdot\mathrm{sr}^{-1}\cdot\mathrm{m}^{-2}$ and sometimes called the spectral radiance, through a slab of thickness z with extinction k_e can be written through the so-called Beer–Lambert–Bouguer approximation law for a collimated beam [54]:

$$I(\mathbf{r}, \hat{\mathbf{s}}) = I(z,\theta,\varphi) = I(0,\theta,\varphi)e^{-\tau(0,z)} = I_0(\theta,\varphi)T_{\mathrm{SS}}(z), \quad (10)$$

where $\mathbf{r}$ is the position vector, $\hat{\mathbf{s}}$ is the direction unit vector along (θ, ϕ) and z is the line-of-sight range, I_0 is the incident intensity upon the slab, and $T_{\mathrm{SS}}(z)$ the single-scattering *transmittance* function (ratio of the received intensity over the incident one for a point receiver) between 0 and the position of the receiver at range z.

The *visibility* range z_V is usually defined, using the third term of Eq. (10), as the range where the transmittance T is equal to a given threshold value t_0; i.e., from the last members of Eq. (10) we have [6]

$$z_V = -\frac{\ln(T_0)}{k_e}. \quad (11)$$

In this work we have considered $T_0 = 0.05$ (or 5%). Usually visibility is defined as being the distance to an object where the image contrast drops to 2% (or 5% according to an alternative definition, e.g., [6]) with respect to the proximity to the same. When attenuation is measured with a 2% threshold at 550 nm, corresponding to the maximum intensity of the solar spectrum, Eq. (11) becomes the Koschmeider formula [7]

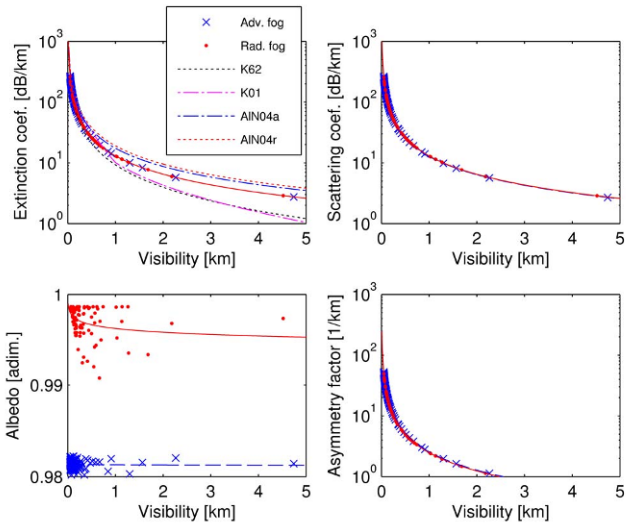

Fig. 10. Same as in Fig. 4, but with respect to visibility V [km]. Extinction panel shows a comparison with the empirical laws due to Kruse *et al.* [55] (K62), Kim *et al.* [56] (K01), and Al Naboulsi *et al.* [57] (AlN04a for advection fog and AlN04r for radiation one).

$z_V = 3.912/k_{e\,550\,\mathrm{nm}}$ with $k_{e\,550\,\mathrm{nm}}$ the extinction coefficient at 550 nm.

The previous equation emphasizes that the visibility is an optical property of the random medium with discrete scatterers and can be defined for any particles whose extinction properties are known (and not only for fog droplets). Figure 10 shows the same as in Fig. 4, but against optical visibility. The extinction coefficient panel also shows a comparison with the empirical laws due to Kruse *et al.* [55], Kim *et al.* [56], and Al Naboulsi *et al.* [57].

Regression parametric models of optical parameters versus optical visibility for all considered particle classes at NIR, using the same power-law model of Eq. (7), but where W_p is replaced by z_V [mm/h], can be derived, but are omitted for brevity.

4. HYDROMETEOR MULTIPLE-SCATTERING EFFECTS

In an absorbing and scattering random medium the Beer law in Eq. (10) must be generalized becoming the radiative transfer equation (RTE), which takes the general integro-differential form for a monochromatic unpolarized radiance. Its full solution requires dedicated numerical techniques, which generally reduce the problem to a set of differential equations in a matrix form with prescribed boundary conditions (e.g., [58]). The precision of these techniques requires a relatively long computational time.

Analytical approaches allow faster solutions of the radiative transfer problem with an acceptable precision, especially considering the uncertainties in the input physical and dielectric parameters intrinsic of many RTE problems. In this work we will adopt the analytical model approach.

A. Radiative Transfer Theoretical Modeling

The Beer–Lambert–Bouguer law can provide an easy estimation of the channel extinction. Unfortunately, it cannot be applied directly in severe weather situations where the multiple scattering by hydrometeors may be significant [25,59,60]. A first-order improvement is represented by modeling the scattering radiation field for the given phase function as produced by a single-scattering event. This approach is valid only for $\tau \ll 1.0$ or $w < 0.5$ (absorbing materials). In an absorbing and scattering random medium, the law in Eq. (10) has to be generalized in the RTE.

The theory of radiative transfer is based on photon transport theory [61], and it is suitable to model the physics of linear beam propagation in the optical wavelength regime only when the interference of waves is negligible. The RTE form for an unpolarized monochromatic radiation in a homogeneous random medium is given by [22]

$$\hat{\mathbf{s}} \cdot \nabla I(\mathbf{r}, \hat{\mathbf{s}}) = \frac{dI(\mathbf{r}, \hat{\mathbf{s}})}{ds} = -k_e I(\mathbf{r}, \hat{\mathbf{s}}) + J(\mathbf{r}, \hat{\mathbf{s}}),$$
$$J(\mathbf{r}, \hat{\mathbf{s}}) = k_s \int_{4\pi} p(\hat{\mathbf{s}}, \hat{\mathbf{s}}') I(\mathbf{r}, \hat{\mathbf{s}}, \hat{\mathbf{s}}') \mathrm{d}\Omega', \tag{12}$$

$I(\mathbf{r}, \hat{\mathbf{s}})$ being the (diffuse) specific intensity and $\nabla I(\mathbf{r}, \hat{\mathbf{s}})$ its gradient at position $\mathbf{r}$ and along direction $\hat{\mathbf{s}}$, related to (θ, ϕ) in spherical coordinates by the direction cosines through $s_x = \sin\theta\cos\phi$, $s_y = \sin\theta\sin\phi$, and $s_z = \cos\theta$. In Eq. (12) ds is the cylindrical elementary volume whose axis is along $\hat{\mathbf{s}}$, $d\Omega$ is the solid angle, $J(\mathbf{r}, \theta, \phi)$ is the source function, and p is the scattering phase function normalized to 1 as deduced from Eq. (3):

$$\int_{4\pi} p(\hat{\mathbf{s}}, \hat{\mathbf{s}}') \mathrm{d}\Omega' = \frac{1}{k_s} \int_{4\pi} k_d(\hat{\mathbf{s}}, \hat{\mathbf{s}}') \mathrm{d}\Omega' = 1. \tag{13}$$

Note that the previous normalization of p may be different from others also used in the literature [22]. For brevity, the dependence on the wavelength is omitted, while thermal emission is assumed to be negligible within the purposes of this work. The term J is sometimes referred to as the *multiple-scattering* source, while the coherent contribution due to an incident collimated e.m. wave (either a plane-wave or a directive beam) along the direction of incidence is assumed as a boundary condition.

Another simplification for the equation of radiative transfer is represented by *small-angle approximation* (SAA), applicable when the dimensions of the scattering particles are larger than to the wavelength: in this case, the wave scattered by a particle is confined in a small angle in the forward direction. For particles small with respect to wavelength and optical distances greater than unity, the SAA model becomes the *radiative diffusion theory* [62]. SAA is expected to also remain valid for the off-axis configuration as long as the scattering angles remain small compared to the angular spread of the scattering phase function; on the contrary, when the beam spread increases, the radiative diffusion theory could be used [62].

Under the SAA, considering that in Cartesian coordinates $\mathbf{r} = [x, y, z]$ and in cylindrical coordinates $\mathbf{r} = [\boldsymbol{\rho}, z]$ with z the line-of-sight axis along the direction of the incident beam, the RTE can be rewritten as [22]

$$\hat{\mathbf{s}} \cdot \nabla_t I(\boldsymbol{\rho}, z, \mathbf{s}) = \mathbf{s} \cdot \frac{\partial I(\boldsymbol{\rho}, z, \mathbf{s})}{\partial \boldsymbol{\rho}} = (s_x \hat{\mathbf{x}} + s_y \hat{\mathbf{y}}) \cdot \frac{\partial I(\boldsymbol{\rho}, z, \mathbf{s})}{\partial \boldsymbol{\rho}}$$
$$= -\frac{\partial I(\boldsymbol{\rho}, z, \mathbf{s})}{\partial z} - k_e I(\boldsymbol{\rho}, z, \mathbf{s})$$
$$+ k_s \int_{-\infty}^{\infty} p(\mathbf{s} - \mathbf{s}') I(\boldsymbol{\rho}, z, \mathbf{s}') \mathrm{d}\mathbf{s}' \tag{14}$$

where ∇_t is the transverse Laplacian operator and $\mathbf{s}$ is the transverse direction vector in Cartesian coordinates (with unit vectors $\hat{\mathbf{x}}$ and $\hat{\mathbf{y}}$ and direction cosines s_x and s_y); $\hat{\mathbf{s}}$ is projected in the plane transverse to z so that for SAA it holds that $d\mathbf{s} = ds_x ds_y \approx \cos\theta d\Omega \approx d\Omega$. In Eq. (14) the phase function and extinction are assumed to be spatially homogeneous, i.e., independent of z, whereas the integration limits can be extended to infinite due to SAA [22]. The use of SAA justifies modeling the angular distribution of the scattered radiance, expressed by the phase function in Eq. (3), by means of a Gaussian function. In addition, it holds that [62]

$$p(\mathbf{s}) = k_s \frac{\alpha^2}{\pi} \exp(-\alpha^2 s^2) \approx k_s \frac{\alpha^2}{\pi} \exp(-\alpha^2\theta^2),$$
$$I(\boldsymbol{\rho}, z = 0, \mathbf{s}) = I_0(\boldsymbol{\rho}, s) = \frac{\beta^2\gamma^2}{\pi^2} \exp(-\beta^2 s^2 - \gamma^2\rho^2), \quad (15)$$

where for SAA $s = \sin\theta \approx \theta$ and α is a phase-function beamwidth constant that can derived from the normalization in Eq. (13), whereas γ and β are the spatial distribution and angular divergence parameters of the incident beam, respectively. In terms of the minimum spot size R_L, it holds that $\gamma = \sqrt{2}/R_L$, whereas in the parabolic approximation $\beta = 2\pi/(\gamma\lambda)$. Finally, in SAA the power per unit area received within the detector's field of view (FOV), i.e., the irradiance, can be computed by

$$N(\boldsymbol{\rho}, z) = \int_{\Delta\theta_v} I(\boldsymbol{\rho}, z, \mathbf{s}) d\mathbf{s}, \quad (16)$$

where $\Delta\theta_v$ is the half-angle FOV (defined as the half-power beamwidth). An open detector is obtained by $\Delta\theta_v \to \infty$.

In recent years, numerous analytical approaches have been proposed to approximate solutions of the RTE. For example, in [10] a Monte Carlo probabilistic method, based on simulating the propagation path traveled by the photons of the transmitted beam, is illustrated. Other approaches belong to the two-stream approximation family, reviewed in [63]. The Eddington approximation is one of these methods, but is inadequate when single scattering is dominant and in the case of a collimated incident beam; in this respect the hybrid Delta–Eddington method is a more accurate analytical solution of the RTE [39,40,63,64].

In this work we have preferred to adopt the approach proposed by Tam and Zardecki (TZ), which consists of determining multiple-scattering correction factors for the Beer–Lambert–Bouguer law given in Eq. (10) [45]. The principal assumption of the TZ solution is a RTE small-angle solution. Indeed, this is the case for rain and fog particles up to the mid-infrared spectral band. The further assumption of the TZ solution is that the laser beam is Gaussian with respect to both spatial and angular variables. The final assumption of the TZ method is that the received power is collected by an open detector (i.e., there is no obstruction to its FOV) placed on the axis of the monochromatic beam (either divergent or collimated). Under the TZ previous assumptions, the received power P_{RX} incident upon the circular azimuthally symmetric detector is given by [45]

$$P_{RX}(z, k_e) = 2\pi \int_0^{R_d} N(\rho, z)\rho d\rho$$
$$= \exp(-zk_e)\{1 - \exp[-R_d^2(z^2/\beta^2 + 1/\gamma^2)]^{-1}\}$$
$$+ \sum_{m=1}^{\infty} \exp(-zk_e) \frac{k_s^m z^m}{m!}[1 - S(m)], \quad (17)$$

where z is the coordinate in the propagation direction, R_d is the detector radius (considered as the minimum spot size of the beam), β is the angular spread, γ is the spatial size of the beam, and k_e and k_s are the volume extinction and scattering coefficients, respectively. In Eq. (17) $S(m)$ is an integral function of the order-m scattering [45].

The expression in Eq. (17) can be used to derive the multiple-scattering transmittance function $T_{\mathrm{MS}}(z)$ in terms of the power ratio:

$$T_{\mathrm{MS}}(z) = \frac{P_{RX}(z, k_e)}{P_{RX}(z = 0, k_e)} = \exp(-k_e z) G(z), \quad (18)$$

where the gain factor G is given by

$$G(z) = \frac{\{1 - \exp[-R_d^2(z^2/\beta^2 + 1/\gamma^2)]^{-1}\}}{1 - \exp(-\gamma^2 R_d^2)}$$
$$+ \frac{\sum_{m=1}^{\infty} \frac{k_s^m z^m}{m!}[1 - S(m)]}{1 - \exp(-\gamma^2 R_d^2)} \quad (19)$$

In Eq. (18) $P_{RX}(z = 0, k_e)$ is the received power detected close to the source (at $z = 0$), i.e., the transmitted power. For a homogeneous medium k_e is constant and, if $k_e \ll 1$, then $T_{\mathrm{MS}}(z)$ is equivalent to the single-scattering transmittance $T_{\mathrm{SS}}(z) = \exp(-k_e z)$, given in Eq. (10). The gain factor $G(z)$ in Eq. (19) is an amplification term that accounts for multiple scattering and beam divergence. In [65] a systematic study of contributions of increasing order of scattering is illustrated.

The SAA solution to the RTE requires the phase function p to be sharply peaked in the forward direction. As shown by [66], phase functions of different shape but with a single peak of fixed width in the forward direction ensure similar results for the on-axis received power. For the off-axis configuration, SAA remains valid when the scattering angles are of the order of the angular spread of the scattering phase function. Note that the TZ method proposed suffers from two limitations [67]. The first is that mathematically the solution can be applied only to calculate the power received by an open detector; fortunately, a detector with a moderate FOV can be considered as open due to the highly peaked nature of the single-scattering phase function. The TZ model of [45] is generalized in [68] for a detector with a variable FOV. The second limitation is the solution accuracy, which is good for a detector placed on the axis of the beam, but small for an off-axis configuration. In this respect, the numerical technique in [67] shows an improvement of the TZ method [45].

B. Effects of Multiple Scattering

The TZ model represents a very flexible and efficient framework where the multiple-scattering (MS) effects of atmospheric particles can be quantified. Moreover, by comparing the single-scattering results with those of TZ we can aim at evaluating

some parametric correction techniques to better discriminate the multiple-scattering contribution. The following numerical simulations are set up for $\lambda = 1550$ nm, $z = 1$ km (scattering slab depth), and $R_d = 1$ cm (detector radius) coincident with the minimum spot size R_L. The single-scattering (SS) extinction and scattering coefficients k_e, k_s have been computed by particle-equivalent water content W_p through Eq. (7) and the coefficients of Table 2.

Since the Beer–Lambert–Bouguer single-scattering model provides a point-receiver single-scattering transmittance $T_{SS}(z)$, we can compare the latter with the corresponding multiple-scattering transmittance $T_{MS}(z)$, which indeed accounts for both single-/multiple-scattering effects and beam divergence. In Fig. 11 we have compared the results derived from the TZ multiple-scattering model at 1550 nm with those from the SS model. As expected, multiple scattering causes an increase of the overall transmittance (i.e., a reduction of apparent attenuation) even if in most conditions it is not so important. The MS effect is especially evident for fog, where the increment is higher than two orders of magnitude for $\tau = 9$ [69], but also heavy rain and dry snow show consistent increments of TZ transmittance with respect to the SS one. Fog droplets are characterized by high concentrations and smaller sizes with respect to wavelength in a Mie scattering regime, whereas heavy rain large drops exhibit an optical scattering regime with a relatively large albedo as well as dry snowflakes of large size whose absorption is quite low.

Multiple-scattering effects can be wavelength dispersive due to the spectral dependence of the particle refractive index and scattering/extinction behavior. Analogously to Fig. 11, Fig. 12 shows the transmittance for the same atmospheric particles, but at $\lambda = 850$ nm. In this case the increment in transmittance due to MS effects is evident for graupel and wet snow, but also for dry snow and heavy rain particles even though it is less remarkable. On the contrary, for fog the transmittance at 850 nm shows a slightly reduced value with respect to the 1550 nm one.

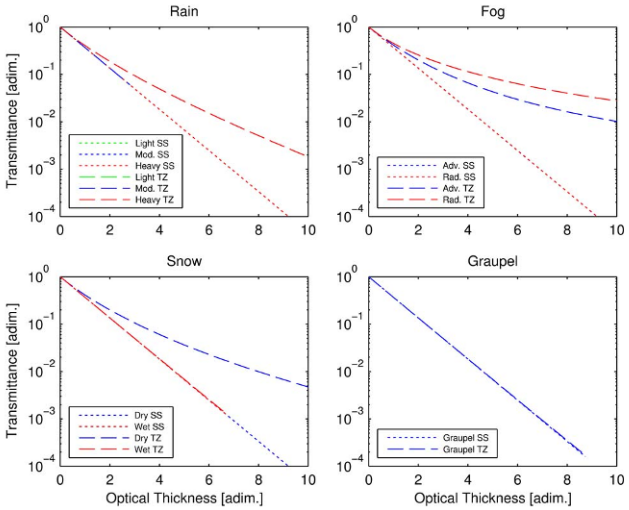

Fig. 11. Transmittance T [adim] along 1 km versus single-scattering (SS) optical thickness τ at 1550 nm for different particles considered in this work (rain, fog, snow, graupel) using the Tam–Zardecki (TZ) multiple-scattering model [45], represented by dashed lines. Single-scattering results lines are shown in colors, but with dotted lines. Note that most lines are nearly coincident with SS, except heavy rain, dry snow, and fog.

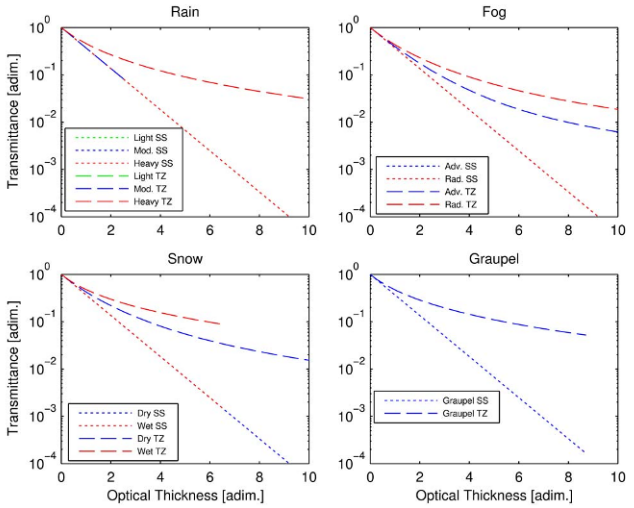

Fig. 12. Same as in Fig. 11 for a wavelength of 850 nm. Note that in this case also TZ wet snow and graupel do not coincide with SS.

By looking at the definitions in Eqs. (10) and (18), it may be worthwhile to introduce the concept of the multiple-scattering equivalent extinction coefficient k_{eMS}. The latter is a volumetric extinction such that, when substituted in $T_{SS}(z)$, it provides the same transmittance value of $T_{MS}(z)$. In other words, it holds that

$$T_{MS}(z) = T_{SS}(z)G(z) \equiv \exp(-k_{eMS}z). \tag{20}$$

Previous definitions can also be transformed in terms of more common path attenuations. In a homogeneous medium we can introduce the single-scattering attenuation A_{SS} [dB] and multiple-scattering attenuation A_{MS} [dB] as

$$\begin{aligned} A_{SS} &= -10\log_{10}[T_{SS}(z)] = 4.343k_e z, \\ A_{MS} &= -10\log_{10}[T_{MS}(z)] = 4.343k_{eMS} z. \end{aligned} \tag{21}$$

Figure 13 shows A_{SS} and A_{MS} at $\lambda = 1550$ nm according to the Tam–Zardecki model and for the atmospheric particles considered here. The plots of A_{SS} and A_{MS} indicate, consistently with what is already shown in Fig. 11, that multiple scattering causes a reduction of apparent attenuation with respect to the single-scattering case, especially for fog and large-size particles such as heavy raindrops and dry snow.

For application purposes, it is worth exploring the correlation between the single-scattering extinction coefficient k_e with respect to the multiple-scattering one k_{eMS}. In this respect we can be interested both in estimating the MS extinction from SS values (e.g., derived from Mie scattering computations) and vice versa (e.g., in the case of apparent extinction measurements to be compared with SS estimates obtained from meteorological data). By adopting the TZ method as a reference numerical solution, for each particle category and wavelength we have found that a fifth-order polynomial functional model is a suitable parametric best fit:

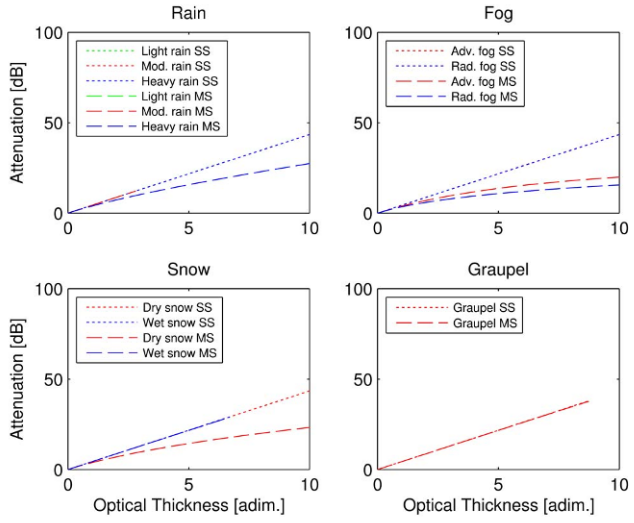

Fig. 13. Single (SS) and multiple (MS) scatteting attenuations, A_{SS} and A_{MS} [dB], with respect to single-scattering optical depth τ [adim.] at 1550 nm for the particles considered in this work and the described Tam and Zardecki model [45].

$$k_{eMS}(\lambda) = \sum_{i=0}^{5} a_i(\lambda)[k_e(\lambda)]^i, \quad k_e(\lambda) = \sum_{i=0}^{5} b_i(\lambda)[k_{eMS}(\lambda)]^i, \tag{22}$$

where a_i and b_i are regression coefficients and k_e and k_{eMS} are expressed in dB/km. Table 3 in Appendix C provides the regression coefficients for k_{eMS} versus k_e in Eq. (22) for five wavelengths at NIR (750, 850, 1064, 1550, and 10,000 nm) for all particle classes listed in Table 1, for k_{eMS}. The reciprocal parametric models for k_e versus k_{eMS} in Eq. (22) can also be derived, but are omitted for brevity.

In order to further investigate and quantify the extra contribution due to multiple-scattering effects, we can also define the multiple-scattering factor $f_{MS}(f)$ as the following ratio:

$$f_{MS} \equiv 1 - \frac{k_{eMS}}{k_e} = 1 - \frac{A_{MS}}{A_{SS}} = 1 - \frac{\ln\lfloor G(z)\rfloor}{A_{SS}}, \tag{23}$$

so that Eq. (20) can be rewritten as

$$T_{MS}(z) = \exp(-k_{eMS}z) = \exp[-k_e(1 - f_{MS})z]. \tag{24}$$

This means that, if $f_{MS} = 0$, multiple scattering is negligible, whereas, if $f_{MS} \to 1$, multiple scattering becomes dominant.

The multiple-scattering factor f_{MS} can be used to highlight the MS effects and parametrize them with respect to atmospheric variables. Indeed, we can combine the definition of f_{MS} with the expression k_{eMS} in Eq. (20) and the dependence of k_e on particle water content W_p in Eq. (7). This leads to

$$f_{MS}(\lambda) = 1 - \frac{\sum_{i=0}^{5} a_i(\lambda)[k_e(\lambda)]^i}{k_e(\lambda)} = 1 - \frac{\sum_{i=0}^{5} a_i(\lambda)[a_{ksp}(\lambda) W_p^{b_{ksp}(\lambda)}]^i}{k_e(\lambda)}, \tag{25}$$

where p stands for the considered particle. Figure 14 shows f_{MS} at 1550 and 850 nm as a function of the water content W_p for

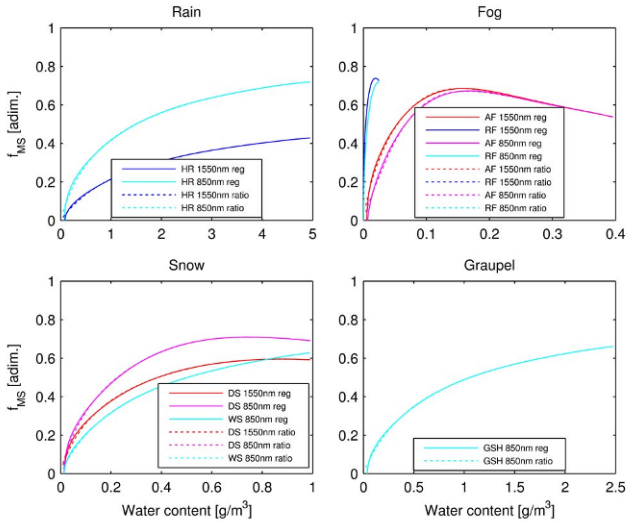

Fig. 14. Multiple-scattering factor f_{MS} at 1550 and 850 nm as a function of water content W_p [g · m^{-3}] for most of the atmospheric particles listed in Table 1. Missing particles are omitted because the multiple-scattering contribution is negligible. Dotted lines indicate f_{MS} as derived from the k_{eMS}/k_e ratio, whereas continuous lines show f_{MS} as obtained through parametric regression given in Eq. (24) (i.e., using a_i and a_{ksp} coefficients). Where dotted lines are superimposed to continuous lines only the latter are visible.

each particle. The factor f_{MS} is generally higher at 850 nm than at 1550 nm wavelength for the same water content, except for fog droplets.

As expected, for the same wavelength, f_{MS} is higher for numerous small droplets and large-size liquid and ice particles. The same figure shows a comparison of f_{MS} as obtained by Eqs. (23) and (25). Polynomial regression provides a fairly good approximation of the f_{MS} ratio.

5. CONCLUSION

FSO technology represents an attractive possibility for wireless communications. The use of narrow optical or NIR beams ensures high data rates with reduced error rates and communication safety. Nevertheless, their sensitivity to atmospheric conditions limits outdoor FSO applications. Fog droplets, but also hydrometeors, may introduce severe path attenuation, which drastically reduces the channel availability. From both modeling and experimental perspectives, several issues are still open.

A unified microphysically oriented line-of-sight propagation model, named MAPS, to simulate particle scattering effects on FSO links has been proposed and developed. Several atmospheric particle classes, such as fog droplets, raindrops, graupel particles, and snowflakes, have been considered. Input data to characterize the water and ice PSDs and particle refractivity have been derived from the available literature and measurements by using a generalized modeling framework. Each particle distribution has been characterized in terms of scattering and absorption coefficients and asymmetry factor as a function of particle water content, fall rate, and visibility.

The validity of the proposed MAPS simulation model spans from visible to infrared wavelengths. Parametric regressive

relations of optical parameters as a function of microphysical quantities have been derived from numerical simulations. The latter are very useful to devise FSO channel models where physically based simple relationships are needed and to explore the potential of new FSO wavelength bands such as infrared links.

Both single- and multiple-scattering effects have also been discussed and quantified by using a small-angle radiative transfer approach. As expected, multiple-scattering effects are significant for fog droplets, but also heavy rain and dry snow show consistent increments of the apparent transmittance with respect to the single-scattering case. This is basically due to higher concentrations and smaller electrical sizes of fog particles in the Mie regime with respect to other hydrometeors. A multiple-scattering factor has also been introduced and parametrized with respect to particle water content for several FSO wavelengths. This result allows us to correct single-scattering simulations in a fairly easy way to take into account multiple-scattering effects.

The proposed MAPS model is affected by some limitations. Nonspherical particles, such as raindrops and snowflakes, should be realistically considered. This aspect should influence the FSO polarization behavior, but also the overall transmittance even though not in a significant way. Multiple-scattering effects might be evaluated with other radiative transfer models in order to overcome the assumption of SAA. Finally, a verification of the proposed MAPS parametrization should be carried out using field experiments where both FSO links and ad hoc meteorological instrumentation are available.

APPENDIX A: SCALED-GAMMA PARTICLE SIZE DISTRIBUTION

The generalized scaled-Gamma (GSG) PSD N_{Gp} [$\mathrm{mm^{-1}\,m^{-3}}$] can be defined as follows:

$$N_{Gp}(r) = N_e \left(\frac{r}{r_e}\right)^{\mu_e} e^{-\Lambda_e \left(\frac{r}{r_e}\right)^{\delta_e}}, \tag{A1}$$

where r [mm] has to be intended as the volume-equivalent spherical particle radius (in order to deal with nonspherical particles as well), r_e [mm] is the effective radius, μ_e and δ_e are the effective shape parameters, N_e is the effective particle number, and Λ_e is the slope parameter. The PSD in Eq. (A1) is called "generalized" as δ_e may be different from one and is scaled as the particle radius is normalized to r_e. Typically δ_e is equal to 1, as assumed hereafter, so that we can refer to Eq. (A1) as simply SG-PSD, indicated by $N_p(r)$ in Eq. (1), where the number of free parameters is only 3, as shown later in [28].

From the knowledge of the particle distribution, shape, and density, Eq. (A1) allows us to introduce some meaningful polydispersion physical parameters. For a spherical particle or sphere-equivalent particle, the *particle mass* m_p [kg] will be given by

$$m_p(r) = \frac{4}{3}\pi\rho_p(r)r^3, \tag{A2}$$

where ρ_p [$\mathrm{g\cdot cm^{-3}}$] is the particle density, which will be assumed independent of radius in the next formulas, if not otherwise stated. Values of ρ_p may range from 0.1 for ice particles to 1 $\mathrm{g\cdot cm^{-3}}$ for pure water particles. If the (incomplete) moment m_n of order n of N_p is expressed by

$$m_n = \int_{r_m}^{r_M} r^n N_p(r)\mathrm{d}r, \tag{A3}$$

where r_m and r_M are the minimum and maximum radius, respectively [70], then the following definitions hold:

- *Total volumetric number* N_t [$\mathrm{m^{-3}}$] of particles, i.e., total number per unit volume, given by

$$N_t = \int_{r_m}^{r_M} N_p(r)\mathrm{d}r = m_0. \tag{A4}$$

- *Water content* W_p [$\mathrm{g\cdot cm^{-3}}$] of sphere-equivalent particles, given by

$$W_p \equiv \int_{r_m}^{r_M} m_p(r)N_p(r)\mathrm{d}r = \frac{4}{3}\pi\rho_p m_3. \tag{A5}$$

- *Effective radius* r_e [mm], defined by

$$r_e = \int_{r_m}^{r_M} r^3 N_p(r)\mathrm{d}r \Big/ \int_{r_m}^{r_M} r^2 N_p(r)\mathrm{d}r = \frac{m_3}{m_2}. \tag{A6}$$

- *Particle fall rate* R_p [$\mathrm{kg\cdot h^{-1}\cdot m^{-2}}$], defined as the particle mass crossing a horizontal cross section of unit area over a given interval of time:

$$R_p = \int_{r_m}^{r_M} v_p(r)m_p(r)N_p(r)\mathrm{d}r = \frac{4\pi}{3}a_v\rho_p m_3 + bv, \tag{A7}$$

where $v_p(r)$ [$\mathrm{m\cdot s^{-1}}$] is the terminal fall velocity in still air of particles (the vertical component of the air speed is assumed zero). The right-hand side of Eq. (A7) is obtained after assuming a power law for v_p dependence on r:

$$v_p(r) = a_v r^{b_v}, \tag{A8}$$

where a_v and b_v are empirical coefficients (which can also take into account the correction for the height-dependent air density). Note that the fall rate can also be expressed by an equivalent height per unit time through $R = R_p/\rho_p$ [mm/h].

Finally, it may be useful to give the explicit expression of the complete moments (i.e., when $r_m = 0$ and $r_M = \infty$) in the case of SG-PSD with $\delta_e = 1$:

$$m_n = \frac{N_e r_e^{n+1}}{\Lambda_e^{n+\mu_e+1}}\Gamma(n+\mu_e+1), \tag{A9}$$

where $\Gamma(\cdot)$ is the complete Gamma function with $\Gamma(n+1) = n!$ if n is an integer. From this general moment, we can express the relation between μ_e and Λ_e as [28]

$$\Lambda_e = \Gamma(\mu_e+4)/\Gamma(\mu_e+3), \tag{A10}$$

and between N_e and W_p, r_e, μ_e, ρ_p as

$$N_e = 10^3 W_p \frac{3\Lambda_e^{4+\mu_e}}{4\pi\rho_p}\frac{1}{r_e^4}\frac{1}{\Gamma(\mu_e+4)}. \tag{A11}$$

In summary, by assuming volume-equivalent spherical particles with density ρ_p and SG-PSD, if the effective radius r_e, the water concentration W_p, and the shape parameter μ_e are specified, we can derive the remaining SG-PSG parameters N_e and Λ_e through Eqs. (A10) and (A11). The particle fall rate R_p can be derived by the water concentration W_p either analytically or by a power law with a_W and b_W regression coefficients:

$$R_p(r) = a_W W_p^{b_W}. \quad \textbf{(A12)}$$

Fog-particle size distribution. A usual choice to describe fog PSD is a Gamma function of the form [29,30,70]

$$N_f(r) = N_{0f} r^{\mu_f} e^{-\Lambda_f r}, \quad \textbf{(A13)}$$

where N_{0f}, Λ_f, and μ_f are known (experimental or modeled) parameters. In order to set up the equivalence relationships between the parameters of SG-PSD in Eq. (A1) and those of the previous expression N_f, it holds that

$$\begin{cases} N_e = N_{0f} r_e^{\mu_f} \\ \Lambda_e = \Lambda_f r_e \\ \mu_e = \mu_f \\ r_e = r_{ef} \end{cases}, \quad \textbf{(A14)}$$

where r_{ef} is the effective radius determined using Eq. (A13) as the PSD. If the fog particle radius r is expressed in [μm], then $\Lambda_e = 10^3 \Lambda_f \cdot r_e$ and $N_e = 10^9 N_{0f} (10^3 r_e)^{\mu_f}$. Note that, from Eq. (A14), the modal radius r_M (defined as the radius corresponding to the PSD maximum) is given by

$$r_M = \frac{\mu_f}{\Lambda_f}. \quad \textbf{(A15)}$$

Rain-particle size distribution. A normalized Gamma function for precipitation-sized hydrometeors generally has the following expression [26,71,72]:

$$N_h(D) = N_{0h}(\mu_h)(D/D_{0h})^{\mu_h} e^{-(3.67+\mu_h)D/D_{0h}}, \quad \textbf{(A16)}$$

where $D = 2r$ is the volume-equivalent spherical particle diameter, N_{0h} is the intercept parameter (which is indeed a function of μ_h [73]), and D_{0h} [mm] is the median volume drop diameter (defined as the diameter corresponding to the 50% of PSD integral). Note that it holds that $N_h(D)dD = N_h(r)dr$ so that $N_h(r) = 2 \cdot N_h(D)$. The equivalence relationships between the parameters of SG-PSD in Eq. (A1) and the parameters of N_h are

$$\begin{cases} N_e = 2N_{0h}(2r_e/D_{0h})^{\mu_h} \\ \Lambda_e = 2r_e(3.67+\mu_h)/D_{0h} \\ \mu_e = \mu_h \\ r_e = r_{eh} \end{cases}, \quad \textbf{(A17)}$$

where r_{eh} is the effective radius determined using Eq. (A16) as the PSD. Note that from Eq. (A16) the mean diameter D_{mh} (defined as the diameter corresponding to the mean of PSD) is given by

$$D_{mh} = \frac{4+\mu_h}{3.67+\mu_h} D_{0h}. \quad \textbf{(A18)}$$

Ice-particle size distribution. An inverse-exponential function of the form is generally used for graupel, small hail, and snow particles [32,72]:

$$N_i(D) = N_{0i} e^{-\Lambda_i D}. \quad \textbf{(A19)}$$

The previous equation corresponds to the Gamma PSD with the shape parameter μ set to zero. Note that from Eq. (A18) the median diameter D_{0i} is given by

$$D_{0h} = \frac{3.67}{\Lambda_i}. \quad \textbf{(A20)}$$

The equivalence relationships between the parameters of SG-PSD in Eq. (A1) and the previous expression are

$$\begin{cases} N_e = 2N_{0i} \\ \Lambda_e = 2\Lambda_i r_e \\ \mu_e = 0 \\ r_e = r_{ei} \end{cases}, \quad \textbf{(A21)}$$

where r_{ei} is the effective radius determined using Eq. (A19) as the PSD.

APPENDIX B: REFRACTION INDEX AND MIXED-PHASE PARTICLES

The complex refraction index $n = n_{re} + jn_{im}$ and the complex permittivity $\varepsilon = \varepsilon_{re} + j\varepsilon_{im}$ of a given material are reciprocally related through (e.g., [74])

$$\begin{cases} \varepsilon_{re} = n_{re}^2 - n_{im}^2, & \varepsilon_{im} = 2n_{re}n_{im} \\ n_{re} = \sqrt{\frac{\sqrt{\varepsilon_{re}^2+\varepsilon_{im}^2}+\varepsilon_{re}}{2}}, & n_{im} = \sqrt{\frac{\sqrt{\varepsilon_{re}^2+\varepsilon_{im}^2}-\varepsilon_{re}}{2}}. \end{cases} \quad \textbf{(B1)}$$

In the presence of a mixture of materials, such as dry snow or wet snow, it is possible to define an effective permittivity of the whole aggregate, where the imaginary part stands for the absorption losses of the mixture. However, supposing a quasi-static approach, the scattering losses are not included in the effective permittivity and we have to consider the obtained solution as a low-frequency one, whose validity is determined by the size of the mixture inclusions and wavelength [36].

Supposing a two-phase mixture of spherical dielectric particles, the Maxwell–Garnett linear formula expresses the effective permittivity ε_{eff} (e.g., [36]):

$$\varepsilon_{\text{eff}} = \varepsilon + \frac{3\varepsilon \cdot f_s(\varepsilon_i - \varepsilon)/(\varepsilon_i + 2\varepsilon)}{1 - f_s(\varepsilon_i - \varepsilon)/(\varepsilon_i + 2\varepsilon)} \quad \textbf{(B2)}$$

with ε_i the complex permittivity of scatterers embedded in a host material of complex permittivity ε and f_s the fractional volume occupied by the scatterers. For spherical inclusions, the maximum packing results in $f_s \cong 0.63$ (see [45]). An example of a two-phase mixture is dry snow, which can be considered to be composed by ice particles embedded within air. It is possible generalize Eq. (B2) to N-phase mixtures [36]:

$$\varepsilon_{\text{eff}} = \varepsilon + \frac{\sum_{j=1}^{N} 3\varepsilon \cdot f_{sj}(\varepsilon_{ij} - \varepsilon)/(\varepsilon_{ij} + 2\varepsilon)}{1 - \sum_{j=1}^{N} f_{sj}(\varepsilon_{ij} - \varepsilon)/(\varepsilon_{ij} + 2\varepsilon)}. \quad \textbf{(B3)}$$

An example of a three-phase mixture is wet snow, which can be modeled as ice and liquid water particles embedded within air.

APPENDIX C: REGRESSION COEFFICIENT TABLES

This appendix contains tables to carry out parametric estimations for FSO applications as a convenient approximation of MAPS results. Regression coefficients for several wavelengths at NIR (750, 850, 1064, 1550, and 10,000 nm) and for all particle classes of Table 1 are given (1) in Table 2 to estimate the optical parameters k_e, k_s, k_a, and $k_s \cdot g$ [km^{-1}] from water content W_p [g · m^{-3}], using formulas given in Eq. (7); and (2) in Table 3 to estimate multiple $k_{e\text{MS}}$ [1/km]-scattering from single k_e [1/km] using $k_{e\text{MS}} = \Sigma a_i k_e^i$ as in Eq. (22).

Table 2. Regression Coefficients to Estimate Optical Parameters k_e, k_s, k_a, and $k_s \cdot g$ [km^{-1}] from Water Content W_p [g · m^{-3}], Using Formulas Given in Eq. (7), for Several Wavelengths at NIR (750, 850, 1064, 1550, and 10,000 nm) for All Particle Classes of Table 1

Wavelength [nm]	Class	a_{kep}	b_{kep}	a_{ksp}	b_{ksp}	a_{kap}	b_{kap}	a_{gp}	b_{gp}
785.00	Light Rain	+4.83E + 00	+1.00E + 00	+4.82E + 00	+1.00E + 00	+4.09E - 03	+1.01E + 00	+4.27E + 00	+1.00E + 00
	Mod. Rain	+4.56E + 00	+9.94E - 01	+4.56E + 00	+9.94E - 01	+5.46E - 03	+1.00E + 00	+4.04E + 00	+9.94E - 01
	Heavy Rain	+3.14E + 00	+1.01E + 00	+3.13E + 00	+1.01E + 00	+5.53E - 03	+9.98E - 01	+2.78E + 00	+1.01E + 00
	Graupel	+3.78E + 00	+1.02E + 00	+3.77E + 00	+1.02E + 00	+7.48E - 03	+1.01E + 00	+3.37E + 00	+1.02E + 00
	Dry Snow	+3.13E + 01	+1.00E + 00	+3.13E + 01	+1.00E + 00	+2.18E - 03	+1.00E + 00	+3.11E + 01	+1.00E + 00
	Wet Snow	+6.54E + 00	+9.79E - 01	+6.51E + 00	+9.78E - 01	+2.40E - 02	+1.03E + 00	+5.79E + 00	+9.74E - 01
	Adv. Fog	+1.56E + 02	+1.01E + 00	+1.56E + 02	+1.01E + 00	+5.64E - 03	+1.00E + 00	+1.35E + 02	+1.01E + 00
	Rad. Fog	+1.13E + 03	+1.01E + 00	+1.13E + 03	+1.01E + 00	+7.96E - 03	+1.05E + 00	+9.44E + 02	+1.01E + 00
850.00	Light Rain	+5.00E + 00	+9.98E - 01	+4.99E + 00	+9.98E - 01	+9.29E - 03	+1.02E + 00	+4.42E + 00	+9.98E - 01
	Mod. Rain	+4.37E + 00	+9.73E - 01	+4.36E + 00	+9.72E - 01	+1.12E - 02	+1.00E + 00	+3.87E + 00	+9.73E - 01
	Heavy Rain	+3.05E + 00	+1.00E + 00	+3.04E + 00	+1.00E + 00	+1.12E - 02	+9.99E - 01	+2.70E + 00	+1.00E + 00
	Graupel	+3.51E + 00	+1.00E + 00	+3.49E + 00	+1.00E + 00	+1.10E - 02	+9.98E - 01	+3.13E + 00	+1.00E + 00
	Dry Snow	+3.13E + 01	+1.00E + 00	+3.13E + 01	+1.00E + 00	+5.52E - 03	+1.00E + 00	+3.11E + 01	+1.00E + 00
	Wet Snow	+6.61E + 00	+9.87E - 01	+6.57E + 00	+9.87E - 01	+4.08E - 02	+1.02E + 00	+5.87E + 00	+9.84E - 01
	Adv. Fog	+1.54E + 02	+1.00E + 00	+1.54E + 02	+1.00E + 00	+1.28E - 02	+1.00E + 00	+1.34E + 02	+1.00E + 00
	Rad. Fog	+7.67E + 02	+9.56E - 01	+7.67E + 02	+9.56E - 01	+1.25E - 02	+9.88E - 01	+6.21E + 02	+9.59E - 01
1064.00	Light Rain	+4.70E + 00	+1.01E + 00	+4.68E + 00	+1.01E + 00	+2.37E - 02	+9.85E - 01	+4.16E + 00	+1.01E + 00
	Mod. Rain	+4.82E + 00	+1.02E + 00	+4.78E + 00	+1.02E + 00	+3.75E - 02	+9.97E - 01	+4.25E + 00	+1.02E + 00
	Heavy Rain	+3.16E + 00	+9.70E - 01	+3.12E + 00	+9.70E - 01	+3.81E - 02	+9.98E - 01	+2.78E + 00	+9.70E - 01
	Graupel	+3.56E + 00	+9.81E - 01	+3.47E + 00	+9.81E - 01	+8.91E - 02	+9.88E - 01	+3.12E + 00	+9.81E - 01
	Dry Snow	+3.13E + 01	+1.00E + 00	+3.13E + 01	+1.00E + 00	+4.48E - 02	+1.00E + 00	+3.11E + 01	+1.00E + 00
	Wet Snow	+6.70E + 00	+1.00E + 00	+6.53E + 00	+1.01E + 00	+1.69E - 01	+9.95E - 01	+5.93E + 00	+1.01E + 00
	Adv. Fog	+1.55E + 02	+1.00E + 00	+1.55E + 02	+1.00E + 00	+4.20E - 02	+1.00E + 00	+1.34E + 02	+1.00E + 00
	Rad. Fog	+6.95E + 02	+9.76E - 01	+6.95E + 02	+9.76E - 01	+4.27E - 02	+9.98E - 01	+5.32E + 02	+9.76E - 01
1550.00	Light Rain	+4.95E + 00	+9.96E - 01	+3.68E + 00	+9.95E - 01	+1.26E + 00	+9.96E - 01	+3.42E + 00	+9.95E - 01
	Mod. Rain	+4.81E + 00	+1.03E + 00	+3.35E + 00	+1.04E + 00	+1.45E + 00	+1.02E + 00	+3.15E + 00	+1.04E + 00
	Heavy Rain	+3.06E + 00	+1.04E + 00	+1.95E + 00	+1.04E + 00	+1.11E + 00	+1.02E + 00	+1.85E + 00	+1.04E + 00
	Graupel	+3.62E + 00	+9.73E - 01	+1.93E + 00	+9.73E - 01	+1.69E + 00	+9.73E - 01	+1.88E + 00	+9.73E - 01
	Dry Snow	+3.14E + 01	+1.00E + 00	+2.59E + 01	+1.00E + 00	+5.48E + 00	+1.00E + 00	+2.58E + 01	+1.00E + 00
	Wet Snow	+6.76E + 00	+1.02E + 00	+3.94E + 00	+1.02E + 00	+2.82E + 00	+1.02E + 00	+3.78E + 00	+1.02E + 00
	Adv. Fog	+1.57E + 02	+1.00E + 00	+1.54E + 02	+1.00E + 00	+2.93E + 00	+1.00E + 00	+1.34E + 02	+1.00E + 00
	Rad. Fog	+7.61E + 02	+8.97E - 01	+7.58E + 02	+8.97E - 01	+2.58E + 00	+9.57E - 01	+6.29E + 02	+8.97E - 01
10000.00	Light Rain	+4.02E + 00	+9.47E - 01	+2.09E + 00	+9.47E - 01	+1.93E + 00	+9.47E - 01	+2.06E + 00	+9.47E - 01
	Mod. Rain	+4.60E + 00	+9.88E - 01	+2.40E + 00	+9.88E - 01	+2.20E + 00	+9.88E - 01	+2.36E + 00	+9.88E - 01
	Heavy Rain	+3.27E + 00	+9.83E - 01	+1.70E + 00	+9.83E - 01	+1.56E + 00	+9.83E - 01	+1.68E + 00	+9.83E - 01
	Graupel	+3.60E + 00	+9.91E - 01	+1.88E + 00	+9.91E - 01	+1.72E + 00	+9.91E - 01	+1.85E + 00	+9.91E - 01
	Dry Snow	+3.16E + 01	+1.00E + 00	+1.59E + 01	+1.00E + 00	+1.57E + 01	+1.00E + 00	+1.59E + 01	+1.00E + 00
	Wet Snow	+6.75E + 00	+9.87E - 01	+3.53E + 00	+9.88E - 01	+3.23E + 00	+9.86E - 01	+3.45E + 00	+9.87E - 01
	Adv. Fog	+1.84E + 02	+1.00E + 00	+1.14E + 02	+1.00E + 00	+6.99E + 01	+1.00E + 00	+1.08E + 02	+1.00E + 00
	Rad. Fog	+2.30E + 02	+9.97E - 01	+1.04E + 02	+9.94E - 01	+1.14E + 02	+9.93E - 01	+6.13E + 01	+9.76E - 01

Table 3. Regression Coefficients of Multiple k_{eMS} [1/km]-Scattering Towards Single k_e [1/km], Using $k_{eMS} = \Sigma a_i k^i$ as in Eq. (22), for Several Wavelengths at NIR (750, 850, 1064, 1550, and 10,000 nm) and for All Particle Classes of Table 1

Wavelength [nm]	Class	a_0	a_1	a_2	a_3	a_4	a_5	RMSE
785	Light rain	+6.41E – 12	–4.30E – 12	+1.04E – 12	–8.84E – 14	+1.00E + 00	+1.03E – 16	+1.52E – 16
	Mod. rain	–6.00E – 06	+4.01E – 07	–1.06E – 04	–1.20E – 03	+1.00E + 00	+2.70E – 07	+1.02E – 07
	Heavy rain	+1.21E – 05	–5.71E – 04	+1.09E – 02	–1.14E – 01	+8.48E – 01	+3.45E – 02	+7.18E – 03
	Graupel	+7.68E – 05	–2.29E – 03	+2.73E – 02	–1.78E – 01	+8.94E – 01	+1.58E – 02	+3.60E – 03
	Dry snow	+3.86E – 07	–5.24E – 05	+2.83E – 03	–6.63E – 02	+8.47E – 01	+6.45E – 02	+1.31E – 02
	Wet snow	+2.94E – 04	–6.12E – 03	+5.17E – 02	–2.43E – 01	+9.30E – 01	+7.67E – 03	+1.76E – 03
	Adv. fog	+1.94E – 07	–3.56E – 05	+2.40E – 03	–6.59E – 02	+9.56E – 01	+1.15E – 01	+6.20E – 02
	Rad. fog	+7.88E – 07	–7.80E – 05	+3.40E – 03	–7.12E – 02	+8.58E – 01	+5.44E – 02	+1.23E – 02
850	Light rain	+8.54E – 12	–6.63E – 12	+2.02E – 12	–2.69E – 13	+1.00E + 00	–1.76E – 16	+1.42E – 16
	Mod. rain	–6.11E – 06	–1.11E – 06	–1.10E – 04	–1.28E – 03	+1.00E + 00	+2.35E – 07	+8.57E – 08
	Heavy rain	+1.43E – 05	–6.52E – 04	+1.20E – 02	–1.18E – 01	+8.39E – 01	+3.53E – 02	+7.30E – 03
	Graupel	+1.07E – 04	–2.93E – 03	+3.22E – 02	–1.93E – 01	+9.00E – 01	+1.39E – 02	+3.14E – 03
	Dry snow	+3.87E – 07	–5.20E – 05	+2.79E – 03	–6.50E – 02	+8.30E – 01	+7.11E – 02	+1.42E – 02
	Wet snow	+2.89E – 04	–6.06E – 03	+5.15E – 02	–2.43E – 01	+9.27E – 01	+7.96E – 03	+1.84E – 03
	Adv. fog	+1.95E – 07	–3.55E – 05	+2.38E – 03	–6.52E – 02	+9.43E – 01	+1.18E – 01	+5.85E – 02
	Rad. fog	+2.32E – 06	–1.61E – 04	+4.90E – 03	–8.03E – 02	+8.43E – 01	+5.16E – 02	+1.09E – 02
1064	Light rain	+9.55E – 12	–6.55E – 12	+1.77E – 12	–2.18E – 13	+1.00E + 00	–1.40E – 16	+1.05E – 16
	Mod. rain	–8.95E – 06	+9.65E – 07	–1.60E – 04	–1.84E – 03	+1.00E + 00	+4.66E – 07	+1.83E – 07
	Heavy rain	+1.57E – 05	–7.06E – 04	+1.26E – 02	–1.20E – 01	+8.24E – 01	+3.82E – 02	+7.61E – 03
	Graupel	+1.11E – 04	–3.01E – 03	+3.29E – 02	–1.94E – 01	+8.95E – 01	+1.45E – 02	+3.19E – 03
	Dry snow	+3.85E – 07	–5.05E – 05	+2.67E – 03	–6.14E – 02	+7.81E – 01	+8.92E – 02	+1.73E – 02
	Wet snow	+2.78E – 04	–5.90E – 03	+5.07E – 02	–2.41E – 01	+9.26E – 01	+8.13E – 03	+1.91E – 03
	Adv. fog	+1.82E – 07	–3.34E – 05	+2.25E – 03	–6.11E – 02	+8.89E – 01	+1.42E – 01	+5.55E – 02
	Rad. fog	+6.12E – 06	–3.39E – 04	+7.75E – 03	–9.59E – 02	+8.15E – 01	+4.97E – 02	+1.01E – 02
1550	Light rain	+4.21E – 12	–3.91E – 12	+1.45E – 12	–2.45E – 13	+1.00E + 00	–4.23E – 16	+1.28E – 16
	Mod. rain	+8.36E – 11	–3.74E – 10	+6.45E – 10	–4.85E – 10	+1.00E + 00	–8.60E – 12	+3.54E – 12
	Heavy rain	+5.74E – 06	–2.90E – 04	+5.91E – 03	–6.67E – 02	+9.38E – 01	+1.57E – 02	+3.67E – 03
	Graupel	–6.49E – 07	+5.85E – 06	–5.22E – 05	–2.87E – 04	+1.00E + 00	+1.58E – 05	+6.02E – 06
	Dry snow	+4.19E – 07	–4.40E – 05	+2.05E – 03	–4.79E – 02	+8.43E – 01	+6.98E – 02	+1.50E – 02
	Wet snow	–8.64E – 07	+4.34E – 06	–4.81E – 05	–5.04E – 04	+1.00E + 00	+4.41E – 06	+1.78E – 06
	Adv. fog	+1.53E – 07	–2.85E – 05	+1.94E – 03	–5.30E – 02	+8.04E – 01	+1.66E – 01	+4.84E – 02
	Rad. fog	+7.11E – 07	–6.96E – 05	+2.98E – 03	–6.01E – 02	+7.13E – 01	+1.07E – 01	+1.95E – 02
10,000	Light rain	+7.33E – 12	–5.06E – 12	+1.38E – 12	–1.71E – 13	+1.00E + 00	+3.26E – 17	+1.19E – 16
	Mod. rain	+3.61E – 10	–1.56E – 09	+2.62E – 09	–1.93E – 09	+1.00E + 00	–3.35E – 11	+1.29E – 11
	Heavy rain	+6.19E – 06	–3.04E – 04	+5.95E – 03	–6.20E – 02	+9.34E – 01	+1.66E – 02	+3.60E – 03
	Graupel	+1.42E – 06	–4.84E – 05	+1.91E – 04	–7.85E – 03	+1.00E + 00	–4.65E – 05	+1.84E – 05
	Dry snow	+5.02E – 07	–4.63E – 05	+1.68E – 03	–3.12E – 02	+8.73E – 01	+5.45E – 02	+1.09E – 02
	Wet snow	+6.67E – 07	–3.50E – 05	+1.05E – 04	–7.60E – 03	+1.00E + 00	–5.85E – 06	+2.30E – 06
	Adv. fog	+2.11E – 08	–5.32E – 06	+5.01E – 04	–1.87E – 02	+7.58E – 01	+1.45E – 01	+2.27E – 02
	Rad. fog	–1.57E – 07	–1.11E – 05	–6.44E – 07	–3.80E – 03	+1.00E + 00	+1.22E – 06	+2.41E – 07

Funding. Sapienza University of Rome (IC1101); Instituto Superiore delle Comunicazioni e delle Tecnologie dell'Informazione (ISCOM) (Ministry of Economic Development).

Acknowledgment. Parametric regressive models, similar to Eq. (7), for all optical parameters with respect to precipitation rate and optical visibility together with parametric models for k_e versus k_{eMS} in Eq. (22) can be provided by the authors upon request at the same wavelengths used in Table 2. N. Kampfer and C. Matzler of Bern University are acknowledged for their support on Mie scattering routines. The authors wish to remember J. A. Weinman and his enthusiastic co-authorship in many projects; his pioneer research on radiative transfer has influenced this study as well—the absence of his precious support is deeply felt.

REFERENCES

1. COST Action IC1101, "Optical wireless communications—an emerging technology," Memorandum of Understanding official document, http://www.cost.eu/COST_Actions/ict/Actions/IC1101, 2011.
2. A. K. Majumdar and J. C. Ricklin, *Free-Space Laser Communications, Principles and Advantages* (Springer, 2008).
3. X. Zhu and J. M. Kahn, "Free-space optical communication through atmospheric turbulence channels," IEEE Trans. Commun. **50**, 1293–1300 (2002).
4. T. H. Carbonneau and D. R. Wisely, "Opportunities and challenges for optical wireless; the competitive advantage of free space telecommunications links in today's crowded market place," in *SPIE Conference on Optical Wireless Communications* (1998), pp. 119–128.
5. M. D'Amico, A. Leva, and B. Micheli, "Free-space optics communication systems: first results from a pilot field-trial in the surrounding area of Milan, Italy," IEEE Microwave Wireless Compon. Lett. **13**, 305–307 (2003).
6. M. S. Awan, R. Nebuloni, C. Capsoni, L. Csurgai-Horva, S. S. Muhammad, F. Nadeem, M. S. Khan, and E. Leitgeb, "Prediction of drop size distribution parameters for optical wireless communications through moderate continental fog," Int. J. Sat. Commun. Netw. **29**, 97–116 (2011).
7. R. Nebuloni, "Empirical relationships between extinction coefficient and visibility in fog," Appl. Opt. **44**, 3795–3804 (2005).
8. S. S. Muhammad, B. Flecker, E. Leitgeb, and M. Gebhart, "Characterization of fog attenuation in terrestrial free space optical links," J. Opt. Eng. **46**, 066001 (2007).
9. F. Nadeem, V. Kvicera, M. S. Awan, E. Leitgeb, S. S. Muhammad, and G. Kandus, "Weather effects on hybrid FSO/RF communication link," IEEE J. Sel. Areas Commun. **27**, 1687–1697 (2009).
10. R. Nebuloni and C. Capsoni, "Effect of hydrometeor scattering on optical wave propagation through the atmosphere," in *Proceedings of the 5th European Conference on Antennas and Propagation (EuCAP)*, Rome, Italy, April 11–15, 2011.
11. H. Henniger and O. Wilfert, "An introduction to free-space optical communications," Radioengineering **19**, 203–212 (2010).
12. F. S. Marzano, S. Mori, F. Frezza, P. Nocito, G. M. Tosi Beleffi, G. Incerti, E. Restuccia, and F. Consalvi, "Free-space optical high-speed link in the urban area of southern Rome: preliminary experimental set up and channel modeling," in *Proceedings of the 11th International Conference on Telecommunications (ConTEL 2011)*, Graz, Austria, June 15–17, 2011.
13. J. Pesek, O. Fiser, J. Svoboda, and V. Schejbal, "Modeling of 830 nm FSO link attenuation in fog or wind turbulence," Radioengineering **19**, 237–241 (2010).
14. V. Kvicera, M. Grabner, and O. Fiser, "Propagation characteristics and availability performance assessment for simulated terrestrial hybrid 850 nm/58 GHz system," Radioengineering **19**, 254–261 (2010).
15. M. S. Awan, E. Leitgeb, S. S. Muhammad, M. Marzuki, F. Nadeem, M. S. Khan, and C. Capsoni, "Distribution function for continental and maritime fog environments for optical wireless," in *Proceedings of Communication Systems Networks and Digital Signal Processing (CSNDSP)*, Graz, Austria, July 23–25, 2008, pp. 260–264.
16. C. Capsoni, N. Nebuloni, and M. D'amico, "Attenuation due to rain on FSO," in *Proceedings of XVI Riunione Nazionale di Elettromagnetismo (RiNEm)*, Genova, Italy, 18–21 September 2006.
17. W. Popoola, Z. Ghassemlooy, M. S. Awan, and E. Leitgeb, "Atmospheric channel effects on terrestrial free space optical communication links," in *Proceedings of Electronics, Computers and Artificial Intelligence (ECAI)*, Pitesti, Romania, July 2–5, 2009.
18. J. Li and M. Uysal, "Achievable information rate for outdoor free space optical communication with intensity modulation and direct detection," in *Proceedings of the Global Telecommunications Conference (GLOBECOM)*, San Francisco, Calif., Dec. 1–5, 2003.
19. M. S. Awan, L. Csurgai Horwath, S. S. Muhammad, E. Leitgeb, F. Nadeem, and M. S. Khan, "Characterization of fog and snow attenuations for free-space optical propagation," J. Commun. **4**, 533–545 (2009).
20. A. Andò, S. Mangione, L. Curcio, S. Stivala, G. Garbo, A. Busacca, G. M. Tosi Beleffi, and F. S. Marzano, "Rateless code performance test on terrestrial FSO time-correlated channel model," in *Proceedings of the International Workshop on Optical Wireless Communications (IWOW)*, Pisa, Italy, October 22, 2012.
21. "Propagation data required for the design of terrestrial free-space optical links," ITU-R Recommendation P.1817-1, 2012.
22. A. Ishimaru, *Wave Propagation and Scattering in Random Media* (IEEE, 1997).
23. F. S. Marzano, D. Scaranari, and G. Vulpiani, "Supervised fuzzy-logic classification of hydrometeors using C-band dual-polarized radars," IEEE Trans. Geosci. Remote Sens. **45**, 3784–3799 (2007).
24. V. N. Bringi and V. Chandrasekar, *Polarimetric Doppler Weather Radar* (Cambridge University, 2001).
25. C. F. Bohren, "Multiple scattering of light and some of its observable consequences," Am. J. Phys. **55**, 524–533 (1987).
26. E. A. Brandes, K. Ikeda, G. Zhang, M. Schönhuber, and R. M. Rasmussen, "A statistical and physical description of hydrometeor distributions in Colorado snowstorms using a video disdrometer," J. Appl. Meteor. Climatol. **46**, 634–650 (2007).
27. E. P. Shettle and R. W. Fenn, "Models for the aerosols of the lower atmosphere and the effects of humidity variations on their optical properties," AFOL-TR-79-0214 (Air Force Geophysics Laboratory, 1979).
28. G. W. Petty and W. Huang, "The modified Gamma size distribution applied to inhomogeneous and nonspherical particles: key relationships and conversions," J. Atmos. Sci. **68**, 1460–1473 (2011).
29. M. Gebhart, E. Leitgeb, S. Sheikh Muhammad, B. Flecker, C. Chlestil, M. Al Naboulsi, F. de Fornel, and H. Sizun, "Measurement of light attenuation in dense fog conditions for FSO applications," Proc. SPIE **5891**, 58910K (2005).
30. D. Deirmendjian, "Far-infrared and submillimeter wave attenuation by clouds and rain," J. Appl. Meteorol. **14**, 1584–1593 (1975).
31. M. Grabner and V. Kvicera, "Analysis of rain effect on free space optical and microwave communication links," in *Proceedings of the 11th International Conference on Telecommunications (ConTEL)*, Graz, Austria, June 15–17, 2011.
32. R. Nebuloni and C. Capsoni, "Laser attenuation by falling snow," in *Proceedings of the 6th International Symposium on Communication Systems, Networks and Digital Signal Processing (CNSDSP)*, Graz, Austria (2008), pp. 23–25.
33. D. J. Segelstein, "The complex refractive index of water," M.S. thesis (University of Missouri, 1981).
34. S. G. Warren and R. E. Brandt, "Optical constants of ice from the ultraviolet to the microwave: a revised compilation," J. Geophys. Res. **113**, D14220 (2008).
35. L. Kou, D. Labrie, and P. Chylek, "Refractive indices of water and ice in the 0.65- to 2.5-μm spectral range," Appl. Opt. **32**, 3531–3540 (1993).
36. A. H. Sihvola and J. A. Kong, "Effective permittivity of dielectric mixtures," IEEE Trans. Geosci. Remote Sens. **26**, 420–429 (1988).

37. C. E. L. Myhre and C. J. Nielsen, "Optical properties of atmospheric fog and cloud droplets collected in the Po valley, Italy," Asian Chem. Lett. **7**, 113–118 (2003).
38. C. F. Bohren and D. R. Huffman, *Absorption and Scattering of Light by Small Particles* (Wiley, 1983).
39. J. H. Joseph, W. J. Wiscombe, and J. A. Weinman, "The delta-Eddington approximation for radiative flux transfer," J. Atmos. Sci. **33**, 2452–2459 (1976).
40. F. S. Marzano and G. Ferrauto, "Generalized Eddington analytical model of azimuthally-dependent radiance simulation in stratified media," Appl. Opt. **44**, 6032–6048 (2005).
41. K. N. Liou, *An Introduction to Atmospheric Radiation* (Academic, 2002).
42. T. S. Chu and D. C. Hogg, "Effects of precipitation on propagation at 0.63, 3.5, and 10.6 microns," Bell Syst. Tech. J. **47**, 723–759 (1968).
43. G. Hanel, "Single scattering albedo, asymmetry parameter, apparent refractive index, and apparent soot content of dry atmospheric particles," Appl. Opt. **27**, 2287–2295 (1988).
44. R. G. Pinnick, S. G. Jennings, P. Chýlek, and H. J. Auvermann, "Verification of a linear relation between IR extinction, absorption and liquid water content of fogs," J. Atmos. Sci. **36**, 1577–1586 (1979).
45. W. G. Tam and A. Zardecki, "Multiple scattering corrections to the Beer–Lambert law. 1. Open detector," Appl. Opt. **21**, 2405–2412 (1982).
46. L. C. Andrews and R. L. Phillips, *Laser Beam Propagation Through Random Media* (SPIE, 2005).
47. D. Atlas and C. W. Ulbrich, "Path- and area-integrated rainfall measurement by microwave attenuation in the 1–3 cm band," J. Appl. Meteorol. **16**, 1322–1331 (1977).
48. R. M. Rasmussen, J. Vivekanandan, J. Cole, B. Myers, and C. Masters, "The estimation of snowfall rate using visibility," J. Appl. Meteorol. **38**, 1542–1563 (1999).
49. S. Y. Matrosov, "Modeling backscatter properties of snowfall at millimeter wavelengths," J. Atmos. Sci. **64**, 1727–1736 (2007).
50. C. Magono and T. Nakamura, "Aerodynamic studies of falling snowflakes," J. Meteorol. Soc. Jpn. **43**, 139–147 (1965).
51. C. Magono, "On the falling velocity of solid precipitation elements," in *Science Reports of the Yokohama National University* (Yokohama National University, 1954), pp. 1–8.
52. R. L. Olsen, D. V. Rogers, and D. B. Hodge, "The aRb relation in the calculation of rain attenuation," IEEE Trans. Antennas Propag. **26**, 318–329 (1978).
53. D. B. Rensch and R. K. Long, "Comparative studies of extinction and backscattering by aerosols, fog, and rain at 10.6 μ and 0.63 μ," Appl. Opt. **9**, 1563–1573 (1970).
54. J. W. Wallace and P. V. Hobbs, *Atmospheric Science—An Introductory Survey*, 2nd ed. (Elsevier, 2006).
55. P. W. Kruse, L. D. McGlauchlin, and R. B. McQuistan, *Elements of Infrared Technology: Generation, Transmission and Detection* (Wiley, 1962).
56. I. Kim, B. McArthur, and E. Korevaar, "Comparison of laser beam propagation at 785 and 1550 nm in fog and haze for optical wireless communications," Proc. SPIE **4214**, 26–37 (2001).
57. M. Al Naboulsi, H. Sizun, and F. de Fornel, "Fog attenuation prediction for optical and infrared waves," Opt. Eng. **43**, 319–329 (2004).
58. B. Mayer and A. Kylling, "Technical note: the libRadtran software package for radiative transfer calculations—description and examples of use," Atmos. Chem. Phys. **5**, 1855–1877 (2005).
59. F. S. Marzano and G. M. Tosi Beleffi, "An analytical multiple scattering model to characterize free-space millimeter-wave and optical links in presence of atmospheric impairments," in *Proceedings of the 7th IEEE, IET International Symposium on Communications Systems, Networks and Digital Signal Processing*, Newcastle, UK, July 21–23, 2010.
60. T. Oguchi, "Electromagnetic wave propagation and scattering in rain and other hydrometeors," Proc. IEEE **71**, 1029–1078 (1983).
61. R. K. Osborn and E. H. Clevens, "Photons transport theory," Ann. Phys. **15**, 105–140 (1961).
62. S. A. W. Gerstl, A. Zardecki, W. P. Unruh, D. M. Stupin, G. H. Stokes, and N. E. Elliott, "Off-axis multiple scattering of a laser beam in turbid media: comparison of theory and experiment," Appl. Opt. **26**, 779–785 (1987).
63. W. E. Meador and W. R. Weaver, "Two-stream approximations to radiative transfer in planetary atmospheres—a unified description of existing methods and a new improvement," J. Atmos. Sci. **37**, 630–643 (1980).
64. E. P. Shettle and J. A. Weinman, "The transfer of solar irradiance through inhomogeneous turbid atmospheres evaluated by Eddington's approximation," J. Atmos. Sci. **27**, 1048–1055 (1970).
65. A. Deepak, U. O. Farrukh, and A. Zardecki, "Significance of higher-order multiple scattering for laser beam propagation through hazes, fogs, and clouds," Appl. Opt. **21**, 439–447 (1982).
66. M. A. Box and A. Deepak, "Limiting cases of the small-angle scattering approximation solutions for the propagation of laser beams in anisotropic scattering media," J. Opt. Soc. Am. **71**, 1534–1539 (1981).
67. K. Altmann, "Forward scattering formula of Tam and Zardecki evaluated by use of cubic sections of spherical hypersurfaces," Appl. Opt. **28**, 4077–4087 (1989).
68. A. Zardecki and W. G. Tam, "Multiple scattering corrections to the Beer-Lambert law. 2: Detector with a variable field of view," Appl. Opt. **21**, 2413–2420 (1982).
69. D. A. Stewart and O. M. Essenwanger, "A survey of fog and related optical propagation characteristics," Rev. Geophys. **20**, 481–495 (1982).
70. A. V. Korolev, G. A. Isaac, J. W. Strapp, and A. N. Nvzorov, "In situ measurements of effective diameter and effective droplet number concentration," J. Geophys. Res. **104**, 3993–4003 (1999).
71. C. W. Ulbrich and D. Atlas, "Extinction of visible and infrared radiation in rain: comparison of theory and experiment," J. Atmos. Ocean. Technol. **2**, 331–339 (1985).
72. J. M. Straka, D. S. Zrnic, and A. V. Ryzhkov, "Bulk hydrometeor classification and quantification using polarimetric radar data: synthesis of relations," J. Appl. Meteorol. **39**, 1341–1372 (2000).
73. G. Vulpiani, F. S. Marzano, V. Chandrasekar, and L. Sanghun, "Constrained iterative technique with embedded neural network for dual-polarization radar correction of rain path attenuation," IEEE Trans. Geosci. Remote Sens. **43**, 2305–2314 (2005).
74. P. S. Ray, "Broadband complex refractive indices of ice and water," Appl. Opt. **11**, 1836–1844 (1972).